Greenland Temperature Response to Climate Forcing during the Last Deglaciation

Citation	Buizert, C., Gkinis, V., Severinghaus, J. P., He, F., Lecavalier, B. S., Kindler, P., . . . Brook, E. J. (2014). Greenland temperature response to climate forcing during the last deglaciation. Science, 345(6201), 1177-1180. doi:10.1126/science.1254961
DOI	10.1126/science.1254961
Publisher	American Association for the Advancement of Science
Version	Accepted Manuscript
Terms of Use	http://cdss.library.oregonstate.edu/sa-termsofuse

Greenland Temperature Response to Climate Forcing during the Last Deglaciation

Authors: Christo Buizert[1]*, Vasileios Gkinis[2, 3], Jeffrey P. Severinghaus[4], Feng He[5], Benoit S. Lecavalier[6], Philippe Kindler[7], Markus Leuenberger[7], Anders E. Carlson[1], Bo Vinther[2], Valérie Masson-Delmotte[8], James W. C. White[3], Zhengyu Liu[5,9], Bette Otto-Bliesner[10] and Edward J. Brook[1]

Affiliations:

[1]College of Earth, Ocean and Atmospheric Sciences, Oregon State University, Corvallis, OR 97331, USA.

[2]Centre for Ice and Climate, Niels Bohr Institute, University of Copenhagen, Denmark.

[3]INSTAAR, University of Colorado, Boulder, CO 80309, USA.

[4]Scripps Institution of Oceanography, UC San Diego, La Jolla, CA 92093, USA.

[5]Center for Climatic Research, Nelson Institute for Environmental Studies, University of Wisconsin, Madison, WI 53706, USA.

[6]Department of Physics and Physical Oceanography, Memorial University, St. John's, Canada.

[7]Division of Climate and Environmental Physics, Physics Institute and Oeschger Centre for Climate Change Research, University of Bern, Bern, Switzerland.

[8]Laboratoire des Sciences du Climat et de l'Environnement, Institut Pierre Simon Laplace (UMR CEA-CNRS-UVSQ 8212), Gif-sur-Yvette, France.

[9]Laboratory for Climate and Ocean-Atmosphere Studies, Peking University, Beijing 100871, China.

[10]Climate and Global Dynamics Division, NCAR, Boulder, CO 80307, USA.

*Correspondence to: buizertc@science.oregonstate.edu

Greenland ice core water isotopic composition ($\delta^{18}O$) provides detailed evidence for abrupt climate changes, but is by itself insufficient for quantitative reconstruction of past temperatures and their spatial patterns. We investigate Greenland temperature evolution during the last deglaciation using independent reconstructions from three ice cores and simulations with a coupled ocean-atmosphere climate model. Contrary to the traditional $\delta^{18}O$ interpretation, the Younger Dryas period was 4.5±2°C warmer than the Oldest Dryas, due to increased CO_2 forcing and summer insolation. The magnitude of abrupt temperature changes is larger in central Greenland (9-14°C) than in the northwest (5-9°C), fingerprinting a North-Atlantic origin. Simulated changes in temperature seasonality closely track changes in the Atlantic overturning strength, and support the hypothesis that abrupt climate change is mostly a winter phenomenon.

The last deglaciation (~19-11 ka before present) is the most recent example of natural global warming and large-scale climate reorganization, providing an exceptional opportunity to study the interaction between different components of the climate system (*1*) and climate sensitivity to changes in radiative forcing (*2*). Much of the regional and global climate variability of this period can be explained as the superposition of two distinct modes (*3*, *4*); a global increase in surface temperature related to increased radiative forcing (Fig. 1C), and an inter-hemispheric redistribution of heat associated with variability in the Atlantic meridional overturning circulation (AMOC) strength (Fig. 1D).

High resolution records of Northern Hemisphere (NH) high-latitude climate are provided by Greenland ice core water isotopic composition ($\delta^{18}O$ and δD), a proxy for local condensation temperature (Fig. 1A). Past water isotopic variations reflect site temperature (T_{site}) to first order (*5*), but are also influenced by changes to the atmospheric hydrological cycle, such as evaporation conditions (*6*, *7*), moisture origin and transport pathways (*8*, *9*) and precipitation intermittency or seasonality (*10*). Assuming a linear $\delta^{18}O$-T_{site} relationship suggests that Greenland climate did not begin to warm until the Bølling onset (14.7 ka), lagging much of the globe and implying a negligible Greenland temperature response to increasing atmospheric CO_2 (*11-14*). Such delayed Arctic warming is hard to reconcile with past sea levels and NH ice sheet extent that indicate substantial ice loss prior to the Bølling (*15*). This paradox is exemplified by lower Greenland Summit $\delta^{18}O$ levels during the Younger Dryas period (YD, 12.8-11.7 ka BP) than during the Oldest Dryas period (OD, 18-14.7 ka BP), despite the rise in boreal summer insolation (Fig. 1B) and a ~50 ppm increase in atmospheric CO_2 (*14*, *16*).

Accurate temperature reconstructions are required to improve our understanding of the mechanisms controlling Greenland climate during the last deglaciation, and to benchmark transient climate simulations (*17*, *18*). Here we circumvent the issues that confound water isotope interpretation by using four independent temperature reconstructions from three ice cores (NEEM, NGRIP and GISP2) (Fig. 1G-I), which we combine with transient general circulation model (GCM) simulations (*4*, *16*, *17*). Our work provides a consistent picture of the temporal, spatial and seasonal trends in the Greenland surface temperature response to external (insolation) and internal (CO_2, AMOC, ice topography) climate forcings during the last deglaciation.

Our primary T_{site} reconstruction method utilizes gas phase $\delta^{15}N$-N_2 data (Fig. 1F), and the inversion of a dynamical firn densification model to find the T_{site} history that optimizes the fit to the $\delta^{15}N$ data through an automated algorithm. The method builds on earlier $\delta^{15}N$ work, in which mostly the abrupt transitions were investigated (*5*, *19-21*). Our approach also allows investigation of T_{site} evolution between abrupt transitions, and robustly quantifies the uncertainty associated with the temperature reconstruction by exploring 216 combinations of densification physics and model parameters at each site. Details on the method are given in Figs. S1-S7 (*22*). For the NGRIP core, a second reconstruction method uses the temperature sensitivity of water isotope diffusion in the firn column (*23*). The isotope diffusion length is calculated along the core from high-resolution $\delta^{18}O$ data using spectral techniques. T_{site} is estimated from the

diffusion length after accounting for firn densification, solid ice diffusion and thinning due to ice flow. We perform a sensitivity study with 2000 reconstructions in which values of four key diffusion model parameters are altered. Both NGRIP reconstructions agree within uncertainty, and we therefore average the results. We further use transient climate simulations performed with the coupled ocean-atmosphere Community Climate System Model version 3 (CCSM3), which have been shown to correctly capture many aspects of deglacial climate history (*4, 11, 16, 17*). The CCSM3 model has an equilibrium climate sensitivity of 2.3°C for a doubling of CO_2 (T31 grid), which is within the range of IPCC estimates (*24*).

First, we investigate the temperature difference between the YD and OD periods. Our reconstruction methods yield an ensemble of T_{site} reconstructions for each site, and we bin the results (Fig. 2A). For comparison, mean annual surface air temperature (SAT) changes from the GCM simulations are marked in black on the horizontal axes. All four reconstructions show that the YD period was warmer than the OD, on average by 4.5 ± 2°C (1σ uncertainty). This contrasts with Summit $\delta^{18}O$, which is more strongly depleted during the YD than the OD (*12, 13*). Our reconstruction is consistent with increased CO_2 and boreal summer insolation during the YD relative to the OD (*16*), as well as NH non-ice core proxy synthesis results (Fig. 1E) that also exhibit a positive YD-OD difference (*11*). CCSM3 reproduces our reconstructed YD-OD warming well, simulating a 5.4°C YD-OD difference averaged over the sites. Transient simulations with an Earth system model of intermediate complexity also find a ~5°C YD-OD temperature difference (*18*). Our reconstructions are thus compatible with current understanding of the role of CO_2 forcing on climate. Additional CCSM3 simulations in which the different climatic forcings are isolated (*4*) suggest that the YD-OD warming due to greenhouse gas forcing is about three times as large as the warming caused by increased insolation (Fig. S9). The T_{site} reconstructions show a poleward enhancement of the YD-OD signal, with warming being largest at the NEEM site. This spatial pattern is also captured in the CCSM3 model response (Fig. 2E). While homogeneous Greenland warming is simulated in response to increased CO_2 or insolation, changes in the Laurentide ice sheet topography induce atmospheric circulation changes which affect N-Atlantic climate and can explain the observed spatial gradient (Fig. S9).

Second, we investigate the abrupt climatic events that are superimposed on the gradual warming of the background climate; the magnitudes of the abrupt warming/cooling (ΔT) at the Bølling (14.7 ka), YD (12.8 ka) and Holocene (11.6 ka) onset are shown in Figs. 2B-D. At all sites ΔT is larger at the Bølling transition than at the Holocene transition. For all three abrupt events ΔT is smallest (5-9°C) in Northwest Greenland (NEEM) and largest (9-14°C) in central Greenland (GISP2). This spatial gradient, which is not reflected in $\delta^{18}O$, is also observed for several Dansgaard-Oeschger events (*19*), suggesting it is a robust feature of abrupt climate change over Greenland. CCSM3 fails to reproduce the timing of the Holocene transition, and underestimates the ΔT magnitude of the Bølling and Holocene transitions by ~20%, and the magnitude of the YD cooling by ~75%. Yet CCSM3 qualitatively captures the observed spatial ΔT gradient. In the simulations, AMOC invigoration at the Bølling onset is associated with maximum SAT change

in the N-Atlantic (Fig. 2F) due to increased northward oceanic heat transport and an associated reduction in sea ice cover (Fig. S10). As a result, the simulated SAT changes are largest for ice core sites closest to the N-Atlantic (i.e., GISP2) and smallest in Northwest Greenland.

In the simulations, AMOC variations are induced by a freshwater forcing to the N-Atlantic, using a meltwater discharge scenario designed to be broadly consistent with available evidence of past sea level, ice sheet extent and meltwater routing (*15*). We recognize that processes other than freshwater may have contributed to, and perhaps even caused, the AMOC and sea ice variations of the deglaciation. Regardless of its cause, AMOC invigoration will result in N-Atlantic warming and a reduction in sea ice cover, which in turn affects the atmospheric circulation and Greenland SAT. Atmosphere-only GCM experiments of N-Atlantic sea ice removal under LGM conditions show a ΔT pattern qualitatively similar to that simulated by CCSM3, suggesting sea ice variability by itself may be sufficient to explain this pattern (*25*). The northward reduction in ΔT magnitude we reconstruct over Greenland is thus likely a fingerprint of the N-Atlantic origin of abrupt climate change, irrespective of the precise roles played by freshwater forcing and AMOC variations.

Our T_{site} reconstructions provide annual mean temperatures, and to investigate seasonal temperature changes we turn to the CCSM3 simulations. Simulated Greenland temperature seasonality is strongly linked to AMOC strength and mean climate state, with large (small) seasonality during periods of weak (strong) overturning (Fig. 3B). Most of the seasonality signal is due to winter (DJF) SAT, which changes more than summer (JJA) SAT (Fig. 3A). The dominance of winter SAT is most clearly manifested during abrupt transitions, where simulated DJF ΔT (marked blue in Figs 2B-D) is much larger than JJA ΔT (orange). This contrasts with the (primarily CO_2-forced) YD-OD warming, for which DJF and JJA warming are nearly identical (within 10% of the mean annual change). Our simulations thus support the hypothesis that abrupt climate change is mostly a winter phenomenon (*25-28*). In the simulations, reduced AMOC strength and attendant heat transport (such as during the YD and OD) results in an extensive N-Atlantic winter sea ice cover (Fig. S10). This extended sea ice, in turn, insulates the atmosphere from the moderating influence of the large oceanic heat capacity, resulting in extremely low winter SAT and increased temperature seasonality over Greenland. Because ablation of land based ice occurs primarily during summer months, summer SAT is the main control on continental ice volume (*26*). If AMOC variability mainly affects winter SAT, as suggested by the CCSM3 simulations, it has only a limited impact on margin positions and ice volume, which may in part explain the paucity of YD moraines found across Greenland (*29*) and the continued sea level rise across the OD and YD intervals (*15*). Our temperature reconstructions, as well as the strong AMOC-seasonality link we simulate, can inform efforts to understand and model Greenland ice sheet evolution during the deglaciation.

The independent reconstructions can be used to investigate non-temperature influences on $\delta^{18}O$. To this end we calculate the effective isotope sensitivity $\alpha_{eff} = \Delta\delta^{18}O_{corr} / \Delta T$, with $\Delta\delta^{18}O_{corr}$ the change in $\delta^{18}O$ (corrected for mean ocean $\delta^{18}O$) associated with temperature change ΔT (Fig.

3D). As in other studies (*5*, *19*, *20*), we find that α_{eff} varies both between sites and in time, showing the limitations of the $\delta^{18}O$ paleothermometer. On average, α_{eff} at NEEM is closest to sensitivity values obtained from the present day spatial $\delta^{18}O$-T_{site} relationship and Rayleigh-type distillation models (*7*). Going southwards α_{eff} decreases, reflecting an increasing net effect of non-temperature influences on $\delta^{18}O$. This meridional gradient in $\delta^{18}O$ bias is further demonstrated by the Dye3 core in south Greenland (Fig. 3C), where the YD-OD $\delta^{18}O$ anomaly is most pronounced. GCM simulations suggest that changes in precipitation seasonality most strongly affect South Greenland, in general agreement with the meridional α_{eff} gradient we observe (Fig. S11B). Moisture tracking in the CCM3 atmospheric GCM (*8*) furthermore suggests an increased relative contribution of (strongly distilled) Pacific vapor during the LGM, which is most pronounced at NEEM (Fig. S11A) – and consistent with the observed stronger glacial $\delta^{18}O$ depletion at NEEM. The apparently stable and high α_{eff} values at NEEM may be caused by compensating $\delta^{18}O$ biases, and do not necessarily imply a more faithful $\delta^{18}O$ paleothermometer. Our T_{site} reconstructions can be used in conjunction with GCM isotope modeling to unravel the ice core water isotopic signals ($\delta^{18}O$, deuterium-excess and ^{17}O-excess), potentially providing constraints on atmospheric circulation changes during the last deglaciation.

In summary, our independent temperature reconstructions reveal the magnitude and spatial structure of deglacial Greenland temperature changes, for which $\delta^{18}O$ by itself does not provide reliable, quantitative information. Our work demonstrates the role of CO_2 in forcing Greenland climate during the last deglaciation, shows a spatial pattern of the abrupt deglacial transitions that fingerprints a North Atlantic origin, and identifies an important connection between AMOC strength and temperature seasonality. These results provide a valuable target to benchmark transient climate model simulations, can help refine estimates of past climate sensitivity, and can provide realistic climate forcing for Greenland ice sheet models during the last deglaciation.

Acknowledgments: This work is dedicated to the memory of our mentor, friend and colleague Sigfús J. Johnsen (1940–2013). We thank Shaun Marcott, David Noone, Julia Rosen, Peter Langen, Inger Seierstad and Jeremy Shakun for fruitful discussions or assistance. Constructive comments by two anonymous reviewers helped improve the manuscript. We acknowledge funding through NSF grant 08-06377 (J.P.S.), the NOAA Climate & Global Change fellowship program, administered by the University Corporation for Atmospheric Research (C.B.), and the US NSF P2C2 program (A.C., Z.L., F.H. and B. O.-B.). This research used resources of the Oak Ridge Leadership Computing Facility, located in the National Center for Computational Sciences at Oak Ridge National Laboratory, which is supported by the Office of Science of the Department of Energy under contract DE-AC05-00OR22725. NEEM is directed and organized by the Center of Ice and Climate at the Niels Bohr Institute and US NSF, Office of Polar Programs. It is supported by funding agencies and institutions in Belgium (FNRS-CFB and FWO), Canada (NRCan/GSC), China (CAS), Denmark (FIST), France (IPEV, CNRS/INSU, CEA and ANR), Germany (AWI), Iceland (RannIs), Japan (NIPR), Korea (KOPRI), The Netherlands (NWO/ALW), Sweden (VR), Switzerland (SNF), United Kingdom (NERC) and the USA (US NSF, Office of Polar Programs). NEEM data and temperature reconstructions are provided as supplementary data files.

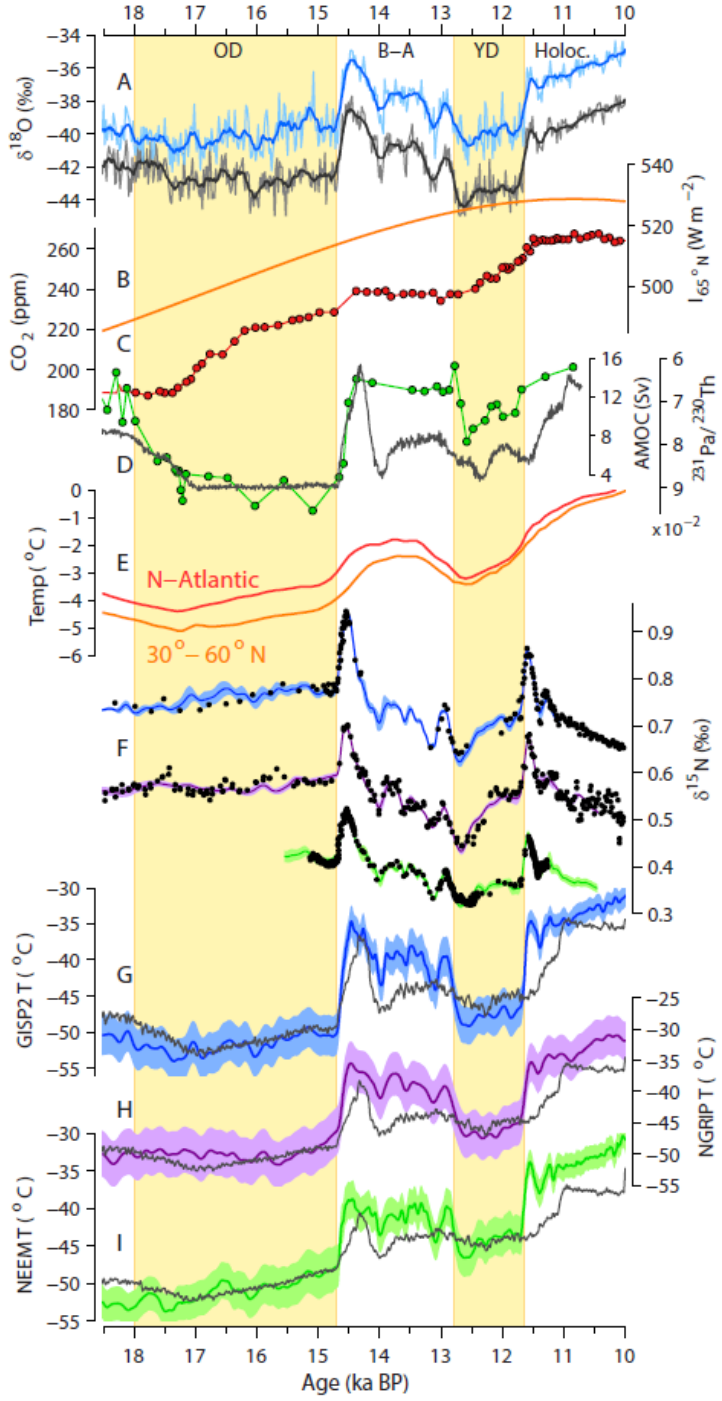

Fig. 1. **Paleoclimate records and Greenland temperature reconstructions for the last deglaciation. (A)** Greenland Summit ice core $\delta^{18}O$ from GISP2 (blue) and GRIP (grey, offset by -3‰ for clarity). **(B)** June 21 insolation at 65°N. **(C)** Atmospheric CO_2 mixing ratios (*14*). **(D)** Bermuda rise (core OCE326-GGC5) $^{231}Pa/^{230}Th$ as a proxy for AMOC strength (green) (*30*), and GCM AMOC strength (grey) in Sv (1 Sv = 10^6 m^3 s^{-1}). **(E)** Surface temperature stacks for 30°N-60°N and North-Atlantic region (*11*). **(F)** GISP2 (blue, offset by +0.3‰ for clarity), NGRIP (purple, +0.15‰ offset) and NEEM (green) model fit to $\delta^{15}N$ data (black dots). **(G-I)** Greenland temperature reconstructions with ±1σ uncertainty envelope for GISP2 (blue), NGRIP (purple) and NEEM (green) and CCSM3 GCM output (grey) (*16, 17*).

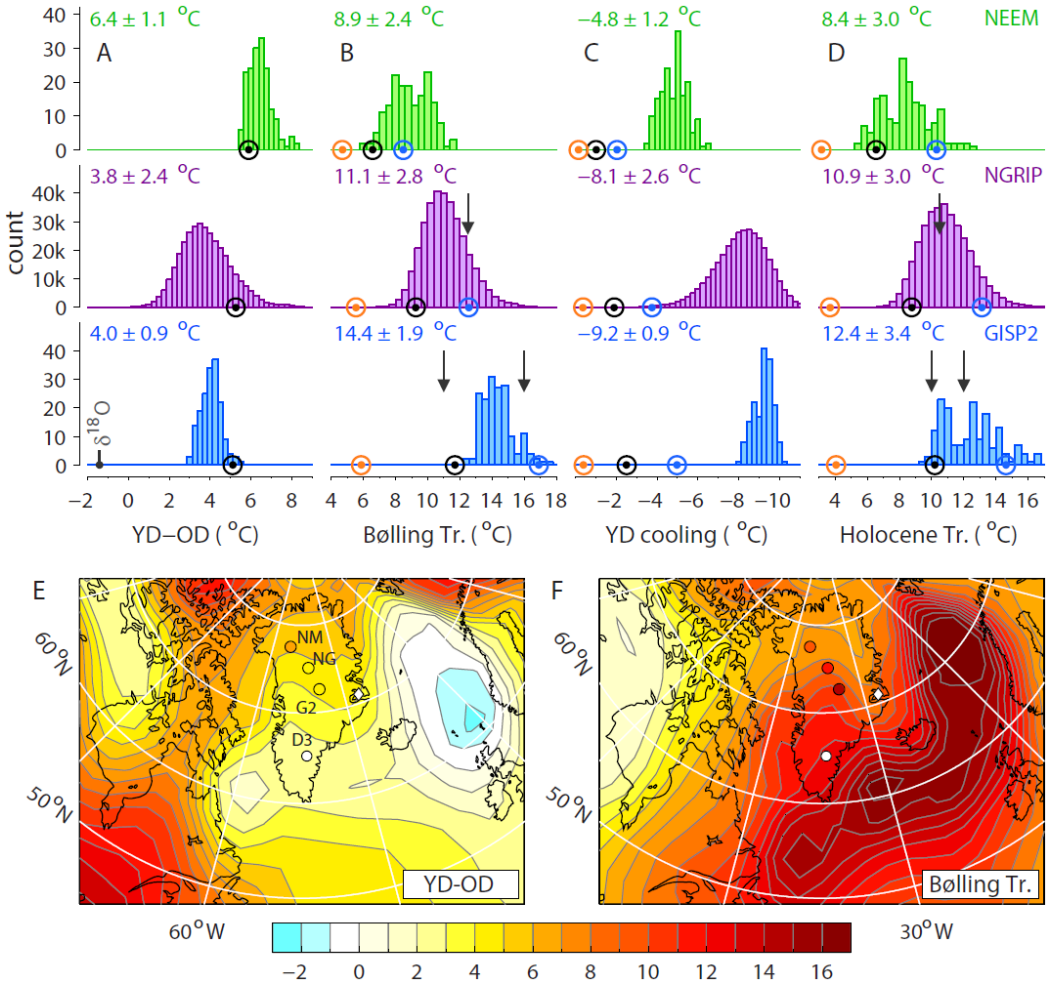

Fig. 2. Spatial patterns in Greenland temperature change. **(A)** Temperature difference between YD and OD. **(B)** Magnitude of Bølling transition. **(C)** Cooling at YD onset. **(D)** Holocene transition. Stated uncertainties give 2σ standard deviation; GCM results are marked in black, orange and blue for mean annual, JJA and DJF, respectively. Published ΔT estimates (arrows) are from refs. (*20, 31-33*). NGRIP values in panels (A) and (C) are potentially impacted by an unexplained abrupt shift in the $\delta^{15}N$ data (Section S1.6). Sensitivity studies suggest that if this shift is due to a calibration error, the $\delta^{15}N$-based YD-OD difference may be 2°C larger, and the YD cooling 2°C smaller in magnitude. **(E-F)** CCSM3 spatial SAT patterns for YD-OD (left panel) and Bølling transition (right panel). Dye 3 and Renland/Scoresby Sund locations are indicated with a white circle and diamond, respectively. NEEM, NGRIP, GISP2 and Dye3 are abbreviated as NM, NG, G2 and D3, respectively. Details on all evaluated time intervals is given in Table S1 (*22*).

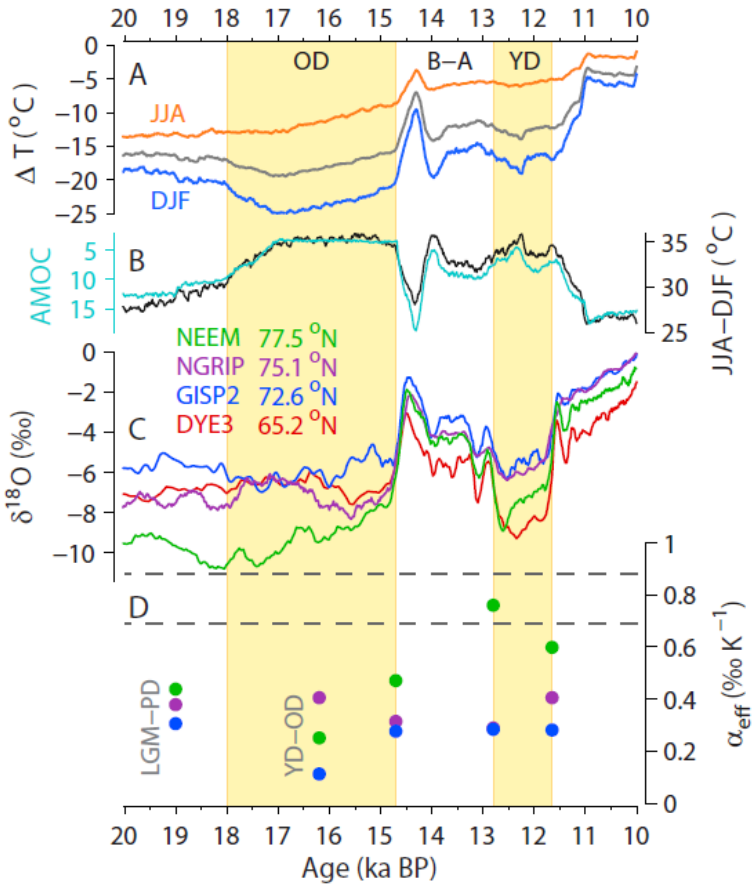

Fig. 3. **Greenland isotopes and temperature seasonality**. **(A)** Simulated summer (JJA), winter (DJF) and mean annual temperatures (grey) relative to present day at Scoresby Sund (see Fig. 2F), the site studied by Denton *et al*. (*26*). **(B)** CCSM3 temperature seasonality JJA-DJF (grey) and AMOC strength in Sv (turquoise). **(C)** $\delta^{18}O$ of four Greenland ice cores corrected for mean oceanic $\delta^{18}O$, relative to present day $\delta^{18}O$. **(D)** Effective isotopic temperature sensitivity for GIPS2 (blue dots), NGRIP (purple) and NEEM (green), with present day spatial isotope sensitivity (0.69 ‰ K^{-1}) and Rayleigh-type distillation model prediction (0.88 ‰ K^{-1}) (dashed lines).

References

1. P. U. Clark *et al.*, Global climate evolution during the last deglaciation. *Proc. Natl. Acad. Sci. U. S. A.* **109**, E1134 (2012).
2. PaleoSENS-project-members, Making sense of palaeoclimate sensitivity. *Nature* **491**, 683 (2012).
3. J. D. Shakun, A. E. Carlson, A global perspective on Last Glacial Maximum to Holocene climate change. *Quat. Sci. Rev.* **29**, 1801 (2010).
4. F. He *et al.*, Northern Hemisphere forcing of Southern Hemisphere climate during the last deglaciation. *Nature* **494**, 81 (2013).
5. C. Huber *et al.*, Isotope calibrated Greenland temperature record over Marine Isotope Stage 3 and its relation to CH(4). *Earth Planet. Sci. Lett.* **243**, 504 (2006).
6. E. A. Boyle, Cool tropical temperatures shift the global delta O-18-T relationship: An explanation for the ice core delta O-18-borehole thermometry conflict? *Geophys. Res. Lett.* **24**, 273 (1997).
7. V. Masson-Delmotte *et al.*, GRIP Deuterium Excess Reveals Rapid and Orbital-Scale Changes in Greenland Moisture Origin. *Science* **309**, 118 (2005).
8. P. L. Langen, B. M. Vinther, Response in atmospheric circulation and sources of Greenland precipitation to glacial boundary conditions. *Clim. Dyn.* **32**, 1035 (2009).
9. C. Charles, D. Rind, J. Jouzel, R. Koster, R. Fairbanks, Glacial-interglacial changes in moisture sources for Greenland: Influences on the ice core record of climate. *Science* **263**, (1994).
10. M. Werner, U. Mikolajewicz, M. Heimann, G. Hoffmann, Borehole versus isotope temperatures on Greenland: Seasonality does matter. *Geophys. Res. Lett.* **27**, 723 (2000).
11. J. D. Shakun *et al.*, Global warming preceded by increasing carbon dioxide concentrations during the last deglaciation. *Nature* **484**, 49 (2012).
12. K. M. Cuffey, G. D. Clow, Temperature, accumulation, and ice sheet elevation in central Greenland through the last deglacial transition. *J. Geophys. Res.* **102**, 26383 (1997).
13. R. B. Alley, The Younger Dryas cold interval as viewed from central Greenland. *Quat. Sci. Rev.* **19**, 213 (2000).
14. E. Monnin *et al.*, Atmospheric CO2 concentrations over the last glacial termination. *Science* **291**, 112 (2001).
15. A. E. Carlson, P. U. Clark, Ice sheet sources of sea level rise and freshwater discharge during the last deglaciation. *Rev. Geophys.* **50**, RG4007 (2012).
16. Z. Liu *et al.*, Younger Dryas cooling and the Greenland climate response to CO2. *Proc. Natl. Acad. Sci. U. S. A.*, (2012).
17. Z. Liu *et al.*, Transient Simulation of Last Deglaciation with a New Mechanism for Bolling-Allerod Warming. *Science* **325**, 310 (2009).
18. L. Menviel, A. Timmermann, O. E. Timm, A. Mouchet, Deconstructing the Last Glacial termination: the role of millennial and orbital-scale forcings. *Quat. Sci. Rev.* **30**, 1155 (May, 2011).
19. M. Guillevic *et al.*, Spatial gradients of temperature, accumulation and delta18O-ice in Greenland over a series of Dansgaard-Oeschger events. *Clim. Past* **9**, 1029 (2013).
20. P. Kindler *et al.*, Temperature reconstruction from 10 to 120 kyr b2k from the NGRIP ice core. *Clim. Past* **10**, 887 (2014).
21. J. P. Severinghaus, E. J. Brook, Abrupt climate change at the end of the last glacial period inferred from trapped air in polar ice. *Science* **286**, 930 (1999).
22. SOM, Materials and methods are available as supplementary materials on Science Online.
23. V. Gkinis, S. B. Simonsen, S. L. Buchardt, J. W. C. White, B. M. Vinther, Water isotope diffusion rates from the NorthGRIP ice core for the last 16,000 years - glaciological and paleoclimatic implications. *Earth Planet. Sci. Lett.* **http://arxiv.org/abs/1404.4201**, (in review).
24. J. T. Kiehl, C. A. Shields, J. J. Hack, W. D. Collins, The Climate Sensitivity of the Community Climate System Model Version 3 (CCSM3). *J. Clim.* **19**, 2584 (2006).
25. C. Li, D. S. Battisti, D. P. Schrag, E. Tziperman, Abrupt climate shifts in Greenland due to displacements of the sea ice edge. *Geophys. Res. Lett.* **32**, L19702 (2005).

26. G. H. Denton, R. B. Alley, G. C. Comer, W. S. Broecker, The role of seasonality in abrupt climate change. *Quat. Sci. Rev.* **24**, 1159 (2005).
27. W. S. Broecker, Abrupt climate change revisited. *Global Planet. Change* **54**, 211 (2006).
28. J. Fluckiger, R. Knutti, J. W. C. White, H. Renssen, Modeled seasonality of glacial abrupt climate events. *Clim. Dyn.* **31**, 633 (Nov, 2008).
29. S. Funder, K. H. Kjaer, K. K. Kjeldsen, C. Ó. Cofaigh, in *Developments in Quaternary Science, Vol. 15,* In J. Ehlers, P. L. Gibbard, P. D. Hughes, Eds. (Elsevier B.V., Amsterdam, The Netherlands, 2011).
30. J. F. McManus, R. Francois, J. M. Gherardi, L. D. Keigwin, S. Brown-Leger, Collapse and rapid resumption of Atlantic meridional circulation linked to deglacial climate changes. *Nature* **428**, 834 (2004).
31. C. Goujon, J. M. Barnola, C. Ritz, Modeling the densification of polar firn including heat diffusion: Application to close-off characteristics and gas isotopic fractionation for Antarctica and Greenland sites. *J. Geophys. Res.* **108**, 18 (2003).
32. J. P. Severinghaus, A. Grachev, B. Luz, N. Caillon, A method for precise measurement of argon 40/36 and krypton/argon ratios in trapped air in polar ice with applications to past firn thickness and abrupt climate change in Greenland and at Siple Dome, Antarctica. *Geochim. Cosmochim. Acta* **67**, 325 (2003).
33. A. M. Grachev, J. P. Severinghaus, A revised +10±4°C magnitude of the abrupt change in Greenland temperature at the Younger Dryas termination using published GISP2 gas isotope data and air thermal diffusion constants. *Quat. Sci. Rev.* **24**, 513 (2005).

Supplementary Material to: *Greenland Temperature Response to Climate Forcing during the Last Deglaciation,* by C. Buizert *et al.*

Table of Contents

S1: Methods: reconstructing Greenland temperature from $\delta^{15}N$

Diffusive transport in the firn column alters the isotopic composition of molecular nitrogen ($\delta^{15}N$-N_2) relative to the overlying atmosphere through gravitational and thermal fractionation (*34-38*). The latter is commonly used to estimate the magnitude of temperature change at abrupt climate transitions (*5, 19, 21, 31-33, 38-40*). The gravitational fractionation contains temperature information as well because firn densification is temperature dependent. However, uncertainties in firn densification physics, past convective zone thickness (*37, 41*) and other modeling parameters make interpretation more challenging. Here we use an inverse method to estimate past temperatures from both thermal and gravitational fractionation of the nitrogen isotopic composition in N_2 ($\delta^{15}N$), combined with a sensitivity study to incorporate uncertainties. This approach allows us to estimate relative temperature changes over abrupt transitions, as well as absolute temperatures. Our approach is similar to a recent work at NGRIP (*20*), but uses three ice coring sites, is highly automated, optimized for the deglaciation, and deals with modeling uncertainties in a more robust way.

S1.1 Data description

The $\delta^{15}N$-N_2 data from GISP2 and NEEM were measured at Scripps Institution of Oceanography and the University of Rhode Island (USA), following procedures described in detail elsewhere (*42, 43*). In short, air was extracted from 10-15 g ice samples using a melt-refreeze technique, and analyzed using dual inlet isotope ratio mass spectrometry (IRMS). Routine analytical corrections are applied. Reported values are replicate averages. NEEM and GISP2 $\delta^{15}N$ data are a combination of new and previously published data (*21, 32, 33, 44, 45*). The $\delta^{15}N$-N_2 data from

NGRIP were measured at the University of Bern (Switzerland) using a continuous melt, continuous flow IRMS method (*46*), and published previously (*20*). Analytical precision is around 0.005‰ and 0.02‰ for the Scripps and Bern data, respectively. NGRIP $\delta^{15}N$ data differ from the NEEM and GISP2 time series by showing a very pronounced 0.04‰ jump within the relatively stable YD (Fig. S7B); we discuss this in more detail in section S1.6.

NGRIP and GISP2 $\delta^{18}O$ data were published and described elsewhere (*47, 48*). NEEM water stable isotope ($\delta^{18}O$) data were measured on 0.55m samples (so-called bag mean) jointly at the Centre for Ice and Climate, Niels Bohr Institute (Denmark) and at Laboratoire des Sciences du Climat et de l'Environnement in Saclay (France), using standard IRMS techniques. Reported values are the averages of both laboratories. NEEM bag mean $\delta^{18}O$ data covering marine isotope stage (MIS) 5e were published elsewhere (*49*). Analytical precision is better than 0.1‰. For the isotope diffusion T_{site} reconstruction method high resolution (5 cm) NGRIP $\delta^{18}O$ data were used (*23*); such data are currently not available for the other coring sites.

S1.2 Firn model description

We use a coupled firn densification- heat diffusion model with three different descriptions of densification physics: a dynamical version of the Herron-Langway model (*50*), the Pimienta-Barnola model (*51, 52*) and the Arnaud model (*31, 53*). The model has 0.5 m spatial depth resolution down to 1000 m, the lower model boundary (*54*). The heat diffusion model uses a Crank-Nicolson scheme to numerically solve the heat diffusion-advection equation and a zero temperature gradient lower boundary condition. The densification and heat diffusion modules have 2 and 0.4 year time steps, respectively; reducing the densification time step to 1 year does not change the output. Δage and $\delta^{15}N$ are simulated at 4 year resolution. Following Schwander et al. (*54*), we use a lock-in density that equals the mean close-off density (*55*) minus 14 kg m^{-3}. Gas ages are calculated using an empirical parameterization based on firn air measurements from 10 sites in the Arctic and Antarctic (*56*). The model allows for including softening of firn with impurity content, as suggested by recent work (*57*).

The forward model uses time series of site temperature (T_{site}) and accumulation (A) as an input, and generates $\delta^{15}N$ and Δage (the ice age-gas age difference) as an output (Fig. S1). We run the model inversely, where we ask the model to find the T_{site} and A history that best fits the $\delta^{15}N$ data (i.e., both the thermal and gravitational components). The initial guess of T_{site} is based on $\delta^{18}O$. The initial guess for A is taken from Cuffey and Clow (1997) for GISP2 (*12*); for NEEM and NGRIP we use annual layer thickness inferred from the GICC'05 depth-age scale corrected for ice flow using a 1-D Dansgaard-Johnsen flow model (*58-60*).

The model makes adjustments to both input functions in order to minimize the root mean square deviation with the $\delta^{15}N$ data:

$$RMSD = \left(\frac{1}{N} \sum_i \frac{(d_i - m_i)^2}{\sigma_i^2} \right)^{\frac{1}{2}} \quad \text{(S1)}$$

where d_i are the data, m_i the interpolated modeled values at the same depth, σ_i the data uncertainty (0.01 ‰ at NEEM and GISP2, and 0.02 ‰ at NGRIP) and N the total number of data points. For each given model configuration the forward model is run 200 times to reach a final solution; the RMSD does not decrease significantly by further increasing the number of model iterations. The same model and inverse method were used elsewhere to derive the ice age-gas age difference (Δage) for the deep NEEM ice core (*59*).

S1.3 Adjustment of T_{site} and A scenarios

Let T_{init} and A_{init} be the initial guess for the temperature and accumulation history of the site, respectively. The final reconstructions are described by:

$$\begin{aligned} T_{site}(t) &= T_{init}(t) \cdot [1 + f_T(t)] \\ A(t) &= A_{init}(t) \cdot [1 + f_A(t)] \end{aligned} \quad \text{(S2)}$$

Our optimization procedure consists of finding the functions f_T and f_A that minimize Eq. (S1). The procedure is illustrated in Fig. S2. We use two series of coefficients, $\{a_i\}$ and $\{b_i\}$ to adjust f_T and f_A, respectively. At the indicated times the f_T and f_A functions are set to equal these coefficients; for the intervals between the time points we linearly interpolate (Figs S2B, C). Through this procedure the problem of adjusting the T and A histories is reduced to adjusting a limited number of coefficients. Coefficient a_4 is omitted for the GISP2 site where $\delta^{15}N$ data is absent during much of the Bølling-Allerød (B-A) interval; coefficient b_7 is set to equal b_6 at NEEM where $\delta^{15}N$ data is absent for the OD interval. In this way the procedure has 5 (6) degrees of freedom to adjust the temperature history at GISP2 (NEEM and NGRIP), and 6 (7) degrees of freedom to adjust the accumulation history at NEEM (GISP2 and NGRIP). Note that the coefficients $\{a_i\}$ were selected to allow the procedure to adjust all major climatic transitions of the deglaciation. The values $\{a_i, b_i\}$ are optimized in an automated gradient method.

T_{init} (in K) was found by converting $\delta^{18}O$ to temperature using a sensitivity α_{init} = 0.43, 0.45 and 0.51 ‰ K^{-1} for GISP2, NGRIP and NEEM, respectively. The α_{init} values were chosen manually to provide a good model fit to $\delta^{15}N$ during the three abrupt cooling events within the B-A period, and agree with published calibrated sensitivities of the paleo-thermometer (*12*, *19-21*, *40*, *61*). It is important to point out that our choice of α_{init} does not influence the key climatic transitions we evaluate in Fig. 2 of the main text: their magnitude is determined by the optimization procedure. These α_{init} values fall within the range of α_{eff} values we derive in the main text (Fig. 3D), and show the same meridional gradient. We apply a moving average to the $\delta^{18}O$ timeseries to reduce noise.

As described above, our initial accumulation estimate A_{init} is based on annual layer thickness estimates and ice flow modeling. These estimates have two main sources of uncertainty. First,

layer counting over this interval is complicated by strong changes in dust loading (by about an order of magnitude) between stadial and interstadial climates. The counting error estimated for the late glacial period is about 5% (*58, 62*). Second, the layer thinning function due to ice flow is derived from simplified 1-D models and is poorly constrained. Borehole logging shows a strong relationship between ice deformation and dust loading (*63*), yet variations in ice rheology are not included in the modeling. Also elevation changes, ice divide migrations and other glaciological complications are not included. Our *A* reconstructions require a reduced glacial accumulation (10-25% reduction between the sites) compared to estimates from layer thinning, in agreement with findings from other $\delta^{15}N$ modeling work (*5, 19, 20, 31*).

S1.4 Sensitivity study

To incorporate the uncertainties inherent to firn modeling we use an ensemble approach where we reconstruct T_{site} for a realistic range of model parameters. We examine the five most important sources of uncertainty:

1. Model physics (3×). We use three different physical descriptions of the densification process: a dynamical version of the Herron-Langway model (*50*), the Pimienta-Barnola model (*51, 52*) and the Arnaud model (*31, 53*). Implementing the first stage of densification ($\rho < 550$ kg m^{-3}) in the Arnaud model proved unsuccessful after several attempts, so for this first stage we use the Herron-Langway description instead; note that this is a small part of the firn column, and does not significantly influence the results.
2. Convective zone (CZ) thickness (4×). The first three scenarios have a static CZ of 0 m, 4 m (roughly present day NEEM conditions (*64*)) and 8 m (twice the present day). Following suggestions that CZ thickness depends on *A* (*41, 65*), we additionally use a scenario where the CZ thickness is given by (12-100·*A*); whenever (12-100·*A*) would be negative, the CZ thickness is set to 0 m instead. This scaling gives a glacial-interglacial CZ contrast of ~ 8 m.
3. Dust softening (3×). Recent work suggests an impurity softening effect in firn (*57*). A first scenario assumes no impurity influence, which is how firn densification has traditionally been modeled. A second scenario includes empirical softening of ice that scales with the logarithm of the Ca^{2+} concentration, where we used Ca^{2+} data from Greenland summit in ppb (*66*). The softening is achieved by multiplying the thermal activation energy (*50, 51, 53*) by the dust softening factor $1-\gamma \ln\left([Ca^{2+}]/[Ca^{2+}_{crit}]\right)$, where $[Ca^{2+}_{crit}] = 0.33$ ng g^{-1} (J. Freitag, personal communication 2012). The sensitivity factor $\gamma = 0.0021$ is determined by fitting density, Δage and $\delta^{15}N$ data from present day Greenland sites (NEEM, GISP2) . In a third scenario we doubled this best-estimate dust sensitivity ($\gamma = 0.0042$) to obtain an upper bound on the influence of dust.
4. Surface density (2×). We use a static surface density of 360 kg m^{-3}, or an existing parameterization in which surface density scales linearly with *A* and *T* (*67*).

5. Initial temperature (3×). We use three scenarios. One assumes the $\delta^{18}O$ thermometer to be reliable throughout the entire 20-14.7 ka interval with constant sensitivity α_{init}; the other two assume a linear deviation from this first scenario by $0^{o}C$ at 14.7ka (the Bølling transition), and $\pm 2^{o}C$ at 20 ka (the beginning of our reconstruction). This is indicated by the dashed lines in Fig. S2b.

We run the inverse model for all permutations of these model settings, yielding a total of 216 (3×4×3×2×3) individual T_{site} reconstructions for each ice core. Rather than trying to select a single "best" solution (which would be as difficult as it is arbitrary), we use the ensemble of solutions in our analysis after discarding the 20% of the solutions with the highest RMSD. A distribution of the RMSD fit of all solutions is shown in Fig. S6A, together with the RMSD cutoff applied to eliminate the 20% of solutions that provide the poorest fit to the $\delta^{15}N$ data. The 20% was chosen because it eliminates the long tail of the RMSD distribution (Fig. S6A). Further analysis shows the exact choice of the cutoff value is of little influence to the key climatic transitions we estimated in the main text (Fig. S6B), and choosing a different value does not alter our conclusions.

S1.5 $\delta^{15}N$-based reconstructions

Figures S3-S5 show the reconstructed temperatures, accumulation rates and the fit to the $\delta^{15}N$ data. The shaded regions show the range of accepted solutions, with the average values shown as dark lines and T_{init} and A_{init} in black (the shaded regions used in Fig 1F-1I of the main text denote $\pm 1\sigma$). We find LGM temperatures consistent with results from borehole thermometry at Greenland summit (*12, 68, 69*). It is important to point out that the temperature reconstructions are constrained by both thermal and gravitational fractionation signals in $\delta^{15}N$, whereas past accumulation rates only influence the gravitational signal. Because the thermal fractionation constrains ΔT across the abrupt transitions very robustly, the T_{site} reconstructions should be considered more reliable than the A reconstructions. For this reason we choose to focus our analysis on the T_{site} reconstructions.

Figures S3-S5A also show the YD and OD averages we use in our analysis as yellow lines. Table S1 gives all the time intervals used in the evaluations. For the Bølling and Holocene transitions we use slightly different intervals in evaluating GCM and T_{site} reconstructions to account for the fact that the transitions are less abrupt, or even delayed, in the GCM simulations; these cases are marked in red in Table S1.

In Fig. S3A we furthermore compared our GISP2 reconstruction to a T_{site} reconstruction for the nearby GRIP site that uses a seasonality correction based on Laurentide ice volume, a T_{source} correction based on deuterium excess (*d*-excess) and a mixed cloud isotopic model (*7*). The latter method finds similar temperatures during the B-A warm period, but warmer temperatures during the glacial period. Note that the *d*-excess correction alone leads to an underestimation of the magnitude of the abrupt transitions, which are robustly constrained by $\delta^{15}N$. This suggests that the $\delta^{18}O$-T_{site} relationship is not stationary in time, and does not only depend on Laurentide ice

volume (*7*). The $\delta^{15}N$ method is based on a relatively simple physical process (gas fractionation in the firn column), that occurs locally at the site and has been widely studied in modern day firn under a wide range of climatic conditions . By contrast, interpretation of the isotopic $\delta^{18}O$ and *d*-excess signatures requires uncertain assumptions regarding atmospheric transport, the hydrological cycle, precipitation seasonality and cloud physics, which render the method more uncertain.

In Figs. 3B-5B we plotted the GCM accumulation rates in red. The accumulation is simulated most successfully for GISP2, and as we go northwards the GCM overestimates the accumulation rates, particularly during the YD interval. Note that we have no NEEM $\delta^{15}N$ data for the early OD period, and consequently NEEM accumulation in that period is not well constrained.

S1.6 Comparison for NGRIP

Figure S7A compares three different temperature reconstructions for NGRIP. The green and red curves show the $\delta^{15}N$-based and isotopic diffusion-based (*23*) reconstructions used in this study, respectively. The black curve shows the average of these two reconstructions, together with a 1σ uncertainty estimate (root sum square of 1σ uncertainties in individual reconstructions) in grey. The blue curve gives a recent temperature reconstruction using the same $\delta^{15}N$ data by Kindler *et al*. (*20*). The latter reconstruction is on average about 3^oC warmer than ours, and consequently we subtracted 3^oC from the Kinder reconstruction in this comparison; note that this does not influence the relative changes in temperature that are the focus of this work. The 3^oC offset is discussed further in section S1.7.

All three reconstructions agree within the estimated 1σ uncertainty envelope. To enable a more quantitative analysis we compare the four climatic transitions discussed in the main text in Table S2. When comparing both $\delta^{15}N$-based reconstructions we find excellent agreement for 3 out of 4 transitions, the exception being the YD cooling (12.8 ka bp) where our method gives more cooling than the Kindler *et al*. method does. The fit of both models to the $\delta^{15}N$ data is shown in Fig. S4C, and indeed the model solutions diverge at the YD onset, with our method providing a slightly better fit than the Kindler *et al*. model. Over the 18.5 ka to 10 ka interval our method obtains an RMSD = 1.01 fit to the $\delta^{15}N$ data, while the Kindler *et al*. model has RMSD = 1.42.

Next we compare the diffusion-based and $\delta^{15}N$-based reconstructions. For the Bølling and Holocene transitions both methods agree with each other well within the uncertainty estimates (Table S2). However, the $\delta^{18}O$ diffusion method finds YD temperatures that are about 4^oC warmer than reconstructed using the $\delta^{15}N$ method (Fig. S7A), and consequently a larger YD-OD temperature difference and a smaller YD cooling (Table S2). We believe that an unusual signal in the NGRIP $\delta^{15}N$ data is the primary cause of this mismatch. Plotting the raw $\delta^{15}N$ timeseries at all three sites (Fig. S7B) reveals that the NGRIP data have a sudden increase within the (relatively stable) YD period that is absent at the other two sites; at 12.5 ka NGRIP $\delta^{15}N$ still

shows the lowest values of all three sites, while at 12.2 ka it has increased to the largest $\delta^{15}N$ values of all three sites. Fig. S4C shows that the firn densification models are unable to reproduce the abruptness of the NGRIP mid-YD $\delta^{15}N$ increase. To obtain such a thick firn column in the late YD, the model requires low YD temperatures (note from Fig. S2 that the algorithm does not have the freedom to change early and late YD temperatures independently). This $\delta^{15}N$ signal could either be due to (highly) anomalous local firn effects, such as a sudden ~8m thinning of the convective zone. Such a rapid convective zone thinning would only be expected in the case of abrupt changes in accumulation or wind speed. There is no evidence for either of these effects in the layer count or dust records, respectively, making this scenario implausible. Alternatively, the $\delta^{15}N$ jump could be a calibration problem in the analytical procedure, as the jump occurred between two separate measurement campaigns. We performed a sensitivity study in which we lowered the $\delta^{15}N$ data between 12.3 to 11.2 ka by 0.035‰ (to correct for putative calibration effects). The result is an increase of ~2^{o}C in the YD temperature, considerably improving the agreement between both reconstruction methods, as well as the agreement with T_{site} reconstructions from the other two sites. In the absence of proof for $\delta^{15}N$ calibration errors we choose to use the original reconstruction; replication of the NGRIP YD $\delta^{15}N$ data is needed to resolve this issue.

The final NGRIP reconstruction is the average of the $\delta^{15}N$-based and diffusion-based (*23*) reconstructions. We resample both NGRIP reconstructions on 10 year intervals using linear interpolation, and then take their mean. The uncertainty on the combined NGRIP reconstruction is the root sum square of the uncertainty on both individual records. In table S2 we give both the arithmetic mean, and the weighted mean for the 4 transitions.

Note that sufficiently high resolution (5 cm) $\delta^{18}O$ data needed for the isotope diffusion method are currently not available for sites other than NGRIP. Consequently we cannot perform the comparison at the NEEM and GISP2 sites.

S1.7 Evaluating potential biases in the $\delta^{15}N$-based reconstructions

The constant offset observed between our $\delta^{15}N$-based reconstruction and that by Kindler *et al*. (Fig. S7) suggests that either method may suffer from a calibration offset. To investigate the offset we test our method under present day conditions at the NEEM, GISP2 and NGRIP sites, where mean annual temperatures are well known. We ask the model to predict *T* and *A* based on $\delta^{15}N$ and Δage at the sites, which is analogous to the paleo situation where Δage is known from comparing the timing (gas phase) thermal fractionation $\delta^{15}N$ warming signal to the (ice phase) $\delta^{18}O$ warming signal (*38*). Note that because the Δage isopleths and $\delta^{15}N$ isoplets run perpendicular to each other in *T, A*-space (Fig. S1), there is a unique solution of *T* and *A* for each combination of Δage and gravitational $\delta^{15}N$.

The present day $\delta^{15}N$ is known from measurements, and the present day Δage and CZ thickness are known from combining firn air pumping experiments with accurate (layer counted) ice age chronologies (*41, 56, 64, 70*). Values are given in Table S3. For all three sites our method correctly predicts the surface temperature within $\pm 0.8^{o}C$. On average, our method underestimates the temperature of the three modern sites by only $0.13^{o}C$, suggesting no systematic bias. Accumulation rates appear to be slightly underestimated (by about 5%). Both the *T* and *A* offset are well within our stated uncertainties. We use Herron-Langway (H-L) firn densification physics in this test (*50*). In our reconstructions we observe no systematic offset between the different formulations of densification physics used (S1.4).

There are two additional lines of evidence that our $\delta^{15}N$ -based reconstructions do not have a systematic bias. First, in terms of absolute temperatures we find good agreement between the $\delta^{15}N$ and diffusion based reconstructions at NGRIP. When subtracting the mean temperature of the $\delta^{15}N$ -based results from the mean temperature of the diffusion-based results, we obtain a difference of $+0.8^{o}C$ for the entire 20-10 ka BP interval, and a difference of $-0.4^{o}C$ for the glacial segment (20-14.7 ka BP). These differences are well within our stated uncertainties, and do not suggest a strong systematic calibration bias in our reconstructions.

Second, our $\delta^{15}N$ method gives LGM (20 ka BP) temperatures around $-50^{o}C$ at all three sites, implying a LGM to present day temperature difference in the 19 ^{o}C to $21^{o}C$ range (using present day observed site temperatures). Reliable, independent estimates of the LGM-present temperature difference can be derived from borehole thermometry; published estimates from this method are $21^{o}C$, $20^{o}C$ and $23^{o}C$, see refs (*12, 68, 69*). Our reconstructions are therefore in good agreement with results from the borehole method. The Kindler *et al*. reconstruction, on the other hand, gives LGM temperatures around $-45.5^{o}C$, implying an LGM-present day temperature difference of only $14.5^{o}C$. Note that due to heat diffusion, the borehole temperature profile cannot be used to directly constrain the YD-OD temperature difference.

The 2013 study by Kindler *et al*. uses an older densification model (*54*), which does not include a convective zone. Sensitivity studies suggest that omitting the convective zone leads to warmer reconstructed temperatures by $1\text{-}2^{o}C$. The impurity enhancement of densification rates that we include furthermore reduces reconstructed temperatures by $1\text{-}2^{o}C$ on average. Combined, these two effects can explain a large fraction of the offset observed between our reconstructions, and those by Kindler *et al*..

S2: Ice sheet surface elevation changes

Our reconstructions give temperature changes at the ice sheet surface, rather than at constant altitude as is desirable for climate reconstructions. Figure S8 shows elevation changes derived by two ice sheet models that include isostatic adjustment of the bedrock with their respective optimal Earth models (*71-74*), with the corresponding temperature change using a surface lapse rate of 7.1°C km^{-1} as observed in present day Greenland climatology (*75*). For the deglaciation

the correction is < 1°C for all sites, which is within the uncertainty of our method. By averaging both elevation models we obtain a correction for the YD-OD temperature difference (Fig. 2A) of +0.4, +0.3 and +0.2 °C for GISP2, NGRIP and NEEM, respectively; for the abrupt transitions the ΔT correction is negligible as the ice sheet responds slowly. Note that the elevation correction would increase the estimated YD-OD temperature difference, making our claim of a warmer YD more robust. However, given the small elevation changes and the uncertainties inherent to ice sheet modeling, we choose not to correct our reconstructions for elevation.

S3: Single-forcing GCM experiments

In order to understand the cause of the poleward enhancement in the YD-OD temperature difference (Fig. 2E) we investigate four single-forcing transient GCM simulations using the fully-coupled CCSM3 model (*4*): the first is forced only with changes in greenhouse gases (GHG, Fig. S9A); the second only with meltwater fluxes from both NH and Antarctic ice sheets (AMOC, Fig. S9B); the third only with variations in the Earth's orbit (ORB, Fig. S9C); and the fourth only with ice sheet topography variations following the ICE-5G (*72*) reconstruction (ICE, Fig. S9D); all remaining forcings are kept constant at their LGM values. The single forcing runs for 22-14.3ka were published by He *et al*. (*4*), here we use extended simulations that include the YD period.

The model runs suggest that the Greenland warming between the OD and the YD is caused by a combination of increased greenhouse gas and insolation forcing (*16*). The former is strong enough to affect the N-Atlantic sea ice cover, leading to enhanced warming due to positive feedbacks mechanisms such as the ice-albedo feedback. During both the YD and OD periods the model AMOC is in a collapsed state (Fig. 1D), and consequently there is no significant temperature response over Greenland when comparing both periods in the AMOC run. Last, the ICE model run shows a strong SAT dipole pattern. Retreat of the Laurentide ice sheet leads to warming over North America, and cooling over much of the N-Atlantic due to changes in planetary waves and more zonal winds than reduce northward transport of warm air. The ICE-5G reconstruction gives only a modest elevation increase over this period (Fig S8), which can explain up to 0.4^{o}C of the modeled Greenland cooling in the ICE model run. In summary, the GCM suggests that the observed poleward enhancement of the YD-OD Greenland warming is a combination of a fairly uniform warming due to increased CO_2 and orbital forcing, which is partly compensated in southern Greenland by a cooling due to retreat of the Laurentide ice sheet.

The Bølling and Holocene transitions are of such short duration that CO_2, insolation and ice sheet topography do not change appreciably; the model attributes the SAT changes over these transitions to AMOC variability.

S4: GCM sea ice changes during the Bølling transition

Sea ice provides a powerful positive climate feedback due to the ice-albedo feedback as well as its ability to insulate the atmosphere from the modulating influence of the high heat capacity of the ocean. Furthermore, sea ice cover can react much more quickly than the oceanic overturning, making it an interesting candidate to explain the abruptness of climatic changes observed in Greenland (*25-27, 76-81*). Figure S10 shows a contour plot of the CCSM3 GCM annual mean sea ice fraction just prior to (panel A), and after (panel B) the Bølling transition. Clearly the Bølling warming is accompanied by a strong reduction in sea ice extent in the model, due to increased northward heat advection upon AMOC resumption. Bølling sea ice extent more closely resembles the present day situation, with much of the north-Atlantic being ice free year round.

The GCM reproduces the observed spatial ΔT gradient for the Bølling transition well (Fig. 2B, F), implying a north-Atlantic origin for the climatic changes. The simulation is forced with variable freshwater fluxes, based on the premise that abrupt transitions are caused by AMOC variability in response to these freshwater perturbations (*17*). A growing body of observational evidence is linking abrupt climate change to reorganizations in ocean circulation (*30, 82-86*). Alternative causes for AMOC variability have been suggested, such as e.g. shifts in wind fields (*87*), ocean-sea ice interactions in the Nordic Seas (*81*), ice shelf collapse (*77*) or Southern Ocean sea ice extent (*88*). Whatever causes the re-invigoration of the AMOC, the warming pattern is likely to resemble that shown in Fig. 2F. Furthermore, an atmosphere-only GCM experiment in which the sea ice cover is removed without an accompanied AMOC resumption finds a similar warming pattern, with the largest SAT increase over the North Atlantic and southeast Greenland (*25*). Therefore we suggest that regardless of the underlying mechanics, any model that invokes AMOC variability, changes in sea ice extent, or a combination thereof to explain abrupt climatic change is likely to produce a ΔT pattern similar to what we observe.

S5: Greenland water isotope sensitivity during the deglaciation

Many parameters other than T_{site} influence the isotopic composition of precipitation (*89*), such as e.g. source temperature (*6*), moisture transport and origin (*7-9, 90-92*) and precipitation seasonality and intermittency (*10, 93-96*). A common approach in ice core literature is to "calibrate" the $\delta^{18}O$ paleo-thermometer using independent estimates of temperature change derived from $\delta^{15}N$ or borehole temperatures (*12, 19, 61, 69*). An unfortunate side effect of this approach is that all abovementioned processes affecting $\delta^{18}O$ are lumped together, and consequently one obtains an "effective" sensitivity α_{eff}, which turns out to be time- and place-dependent (*19, 20*).

Two of the main non-temperature influences on $\delta^{18}O$ are vapor origin and changing precipitation seasonality. Changes in precipitation origin (Fig. S11A) were simulated using the CCM3 atmospheric GCM with moisture tracking functionality, coupled to a slab ocean forced with CLIMAP (*97*) sea surface temperature (SST) estimates (*8*). Only the three dominant sources are

shown; full results can be found in the original study (*8*). Under LGM conditions North-American sources are strongly reduced relative to present day (CTRL) due to the presence of the Laurentide ice sheet. The model suggests that during the LGM the relative contribution of (strongly distilled) Pacific vapor increased – the increase is strongest at NEEM and weaker to the South. At the same time the relative contribution of (lightly distilled) Atlantic vapor decreased – the decrease being small at Dye3 compared to central and northern Greenland. In a qualitative sense, the GCM results suggest that the $\delta^{18}O$ bias introduced by vapor changes would have a meridional gradient, with the bias at NEEM being most negative, and at Dye3 most positive, in agreement with observations (Fig 3C of main text). It is important to point out, however, that different atmospheric models may simulate different changes in precipitation origin (*9, 98*).

Figure S11B shows changes in precipitation seasonality from the atmospheric CCM3 model (black), and the fully coupled CCSM3 model used in this study (red). The seasonality is expressed as the ratio of winter (DJF) to summer (JJA) precipitation. Both models suggest present day summer precipitation exceeds winter precipitation at all three sites, yet the dominance of summer precipitation is greatest at the northern NGRIP and NEEM sites, as also suggested elsewhere (*99*). Evaluation of present day precipitation seasonality is complicated by snow drift and (thermally activated) densification, and no reliable data are available for these sites (*8, 75*). It must be pointed out that the present day DJF/JJA ratio of 0.1 at NEEM as found in the CCM3 model is too low (*99*). Modeled seasonality for the glacial period (LGM, OD) generally indicates winter precipitation is further reduced, with the exception of the NEEM and NGRIP sites in the CCM3 model where the relative contribution of winter precipitation is actually enhanced. Despite their differences, CCM3 and CCSM3 consistently show the largest reduction in glacial winter precipitation at Dye3, which is expected to bias the $\delta^{18}O$ towards summer (i.e., positively). The smallest reduction, or even an increase, in winter precipitation is simulated at NEEM, resulting in a minimal $\delta^{18}O$ seasonality bias.

Ice core $\delta^{18}O$ is generally considered to be a precipitation weighted temperature proxy (*96, 100*). In Fig. S11C we show the GCM simulated mean annual GISP2 temperatures (blue), as well as the simulated precipitation weighted temperatures (orange). The orange curve uses monthly data in the precipitation weighting, for the orange dots daily data were used (6 snapshots of 50 years). We subtracted $5^{o}C$ from the daily weighted averages to make them overlap with the monthly values, suggesting that (overcast) days with high precipitation tend to be about $5^{o}C$ warmer than days without precipitation. Model results are very similar for all sites, and we decided to focus on GISP2, where the best agreement is obtained between the simulated precipitation amount and our reconstruction (Figs. S3-S5). We first note that precipitation weighted temperatures are higher than the mean annual temperatures because GCM precipitation is highest during the (warm) summer months. All the abrupt transitions, clearly visible in winter and annual mean temperature, are strongly muted in the precipitation weighted temperature. The reason for the muted response is that the fraction of annual precipitation occurring during winter (ratio of DJF to annual precipitation) is strongly correlated with winter temperatures (r = 0.95) in the CCSM3

simulations. During abrupt warming events, the model produces an increase in the amount of winter precipitation, which therefore damps the magnitude of warming in the precipitation weighted temperature.

Surprisingly, the GCM precipitation weighted temperatures deviate more strongly from the Greenland $\delta^{18}O$ isotopic records than the simulated annual mean temperatures do, even though the ice core records are thought to represent a precipitation weighted signal. This discrepancy may arise from inaccuracies in the simulated precipitation seasonality, which will skew the precipitation weighting. Alternatively, the water isotopic signals recorded in ice cores may have been subject to alteration after initial snow deposition. A recent study has demonstrated that surface snow isotopic composition can change in between snowfall events in response to changes in air mass trajectories (*101*). So far, these vapor exchange effects are not yet modeled, and their amplitude has not been accurately assessed. If post-depositional vapor exchange dominates the recorded $\delta^{18}O$ signal, this could result in a closer relationship between $\delta^{18}O$ and annual mean temperature than between $\delta^{18}O$ and precipitation weighted temperature. Finally, a direct comparison of precipitation weighted temperatures with $\delta^{18}O$ records neglects changes in moisture source conditions and transport pathways, that are known to affect the $\delta^{18}O$ of precipitation (*6*, *7*).

This analysis highlights many of the complications in traditional $\delta^{18}O$ interpretation, demonstrating the importance of independent temperature reconstructions.

S6: Tables and Figures

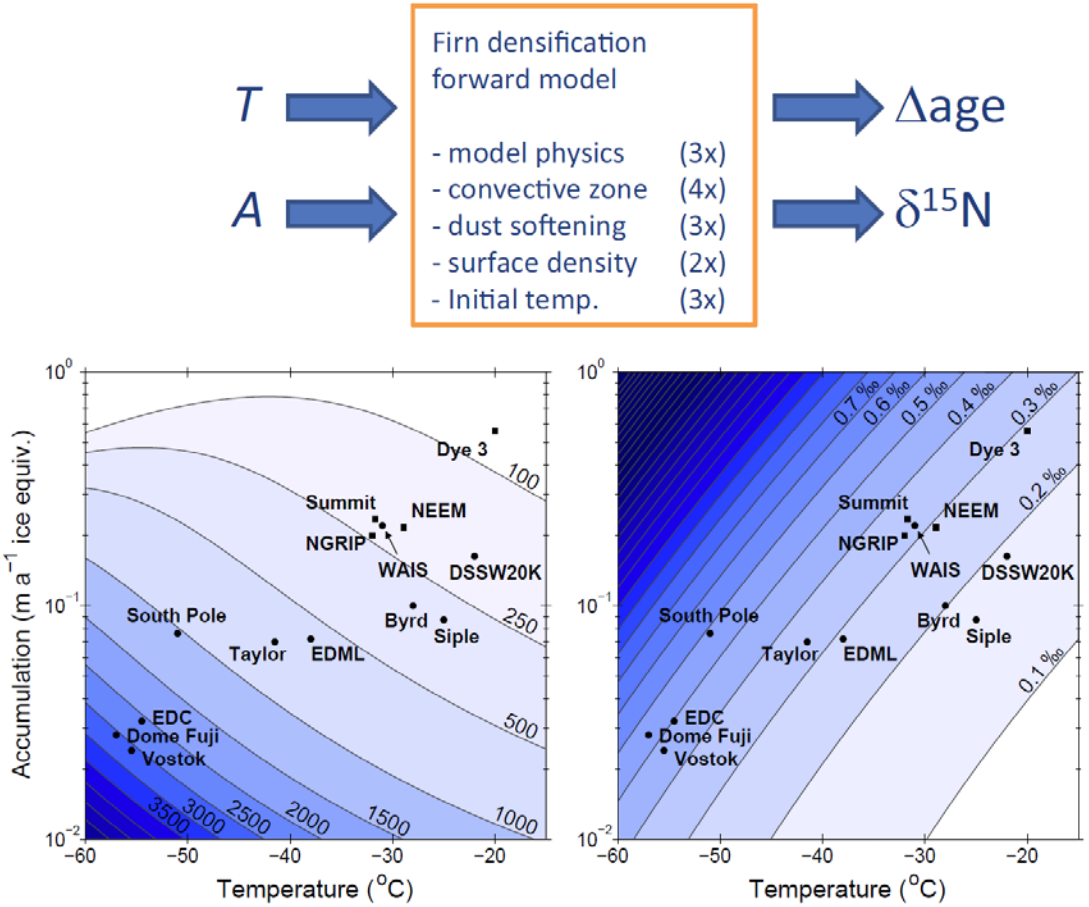

Figure S1: Firn densification modeling. Upper panel shows the schematic of the forward model with input (*A*, *T*) and output (Δage, $\delta^{15}N$). Listed model parameters are varied in the sensitivity study; the number in parenthesis indicates how many values were included (see text). Lower panels show contour lines of equal Δage (left) and equal gravitational $\delta^{15}N$ (right) under equilibrium climatic conditions (*T*, *A*) using the steady state Herron-Langway model (*50*) and a lock-in density that equals the mean close-off density from Martinerie *et al.* (*55*) minus 14 kg m^{-3}.

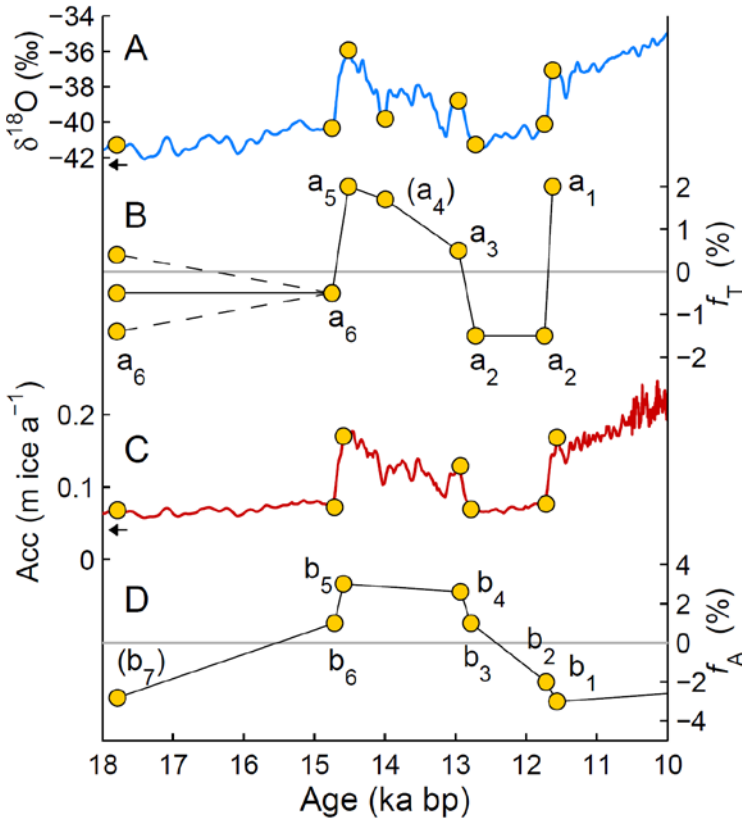

Figure S2: T_{site} and A reconstruction in an inverse modeling approach. (A) $\delta^{18}O$ profile used for T_{init} estimation with position of adjustment points. **(B)** Adjustment function f_T in percent with adjustment coefficients $\{a_i\}$. **(C)** A_{init} from layer thinning with adjustment points. **(D)** Adjustment function f_A in percent with adjustment coefficients $\{b_i\}$.

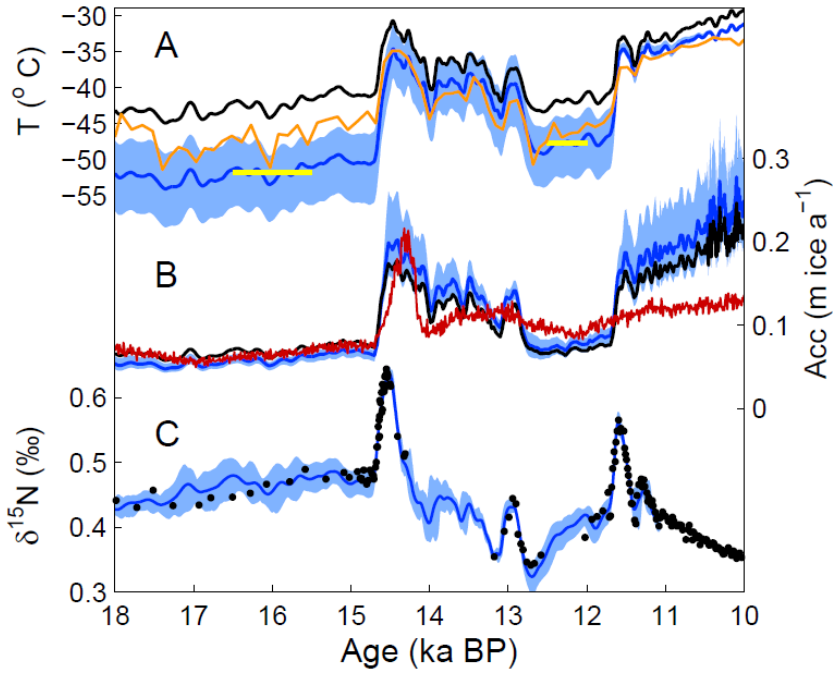

Figure S3: δ^{15}N-based T_{site} reconstruction for GISP2. (A) Range of T_{site} estimates (shaded region) with mean (dark blue line), T_{init} (black line), T_{site} reconstruction from Masson-Delmotte *et al*. (orange line) (*7*) and OD/YD averages (yellow horizontal lines). A comparison to GCM simulated temperatures is shown in Fig. 1 of the main text. **(B)** Range of *A* estimates (shaded region) with mean (dark blue line), A_{init} (black line) and GCM accumulation (red line). **(C)** Range of δ^{15}N model solutions (shaded region) with mean (dark blue line) and δ^{15}N data (black dots).

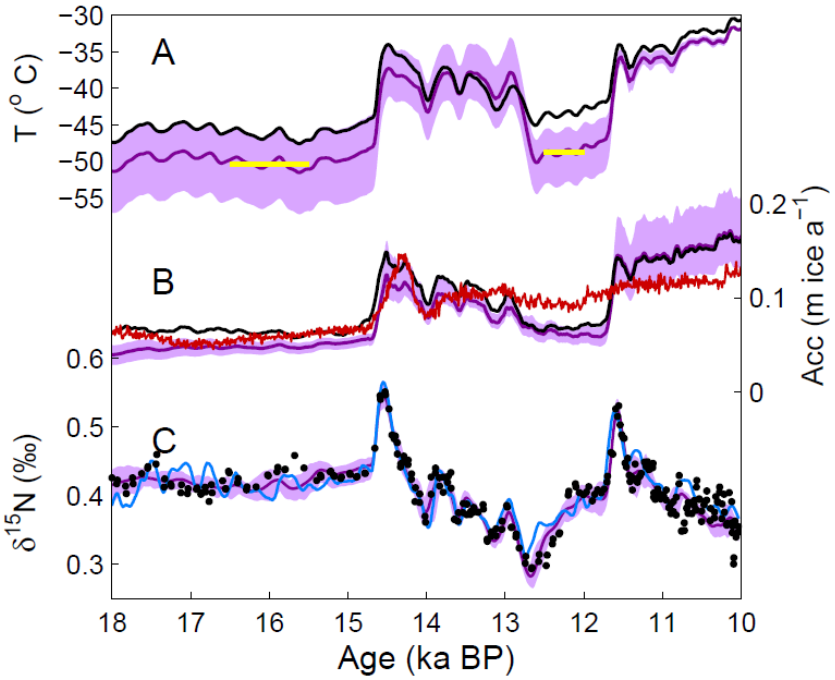

Figure S4: δ^{15}N-based T_{site} reconstruction for NGRIP. (A) Range of T_{site} estimates (shaded region) with mean (dark purple line), T_{init} (black line) and and OD/YD averages (yellow horizontal lines). A comparison to GCM simulated temperatures is shown in Fig. 1 of the main text. **(B)** Range of *A* estimates (shaded region) with mean (dark purple line), A_{init} (black line) and GCM accumulation (red line). **(C)** Range of δ^{15}N model solutions (shaded region) with mean (dark purple line), model simulation from Kindler *et al*. (blue line) (*20*) and δ^{15}N data (black dots); Kindler *et al*. results were transferred from the SS09 to the GICC'05 chronology used in this study.

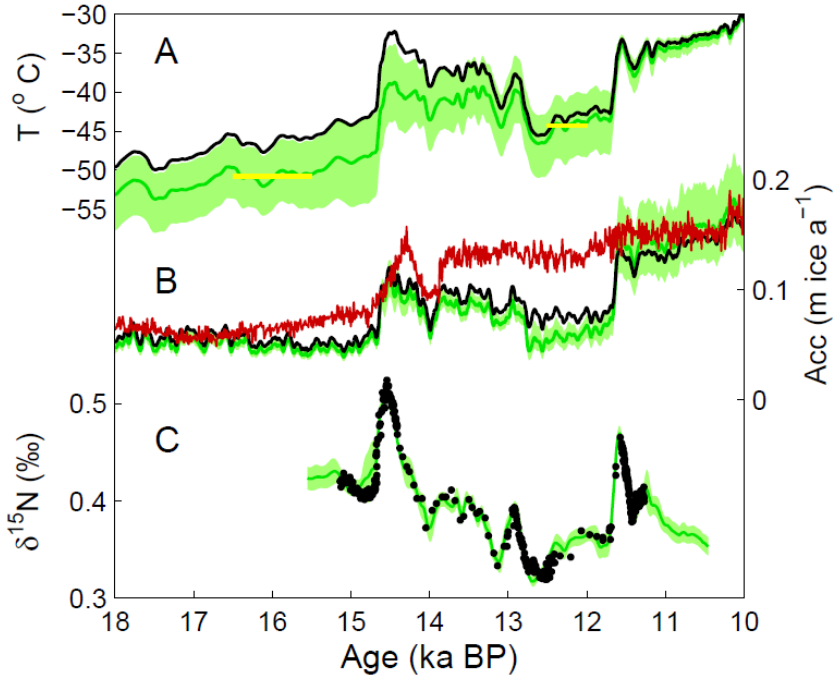

Figure S5: δ^{15}N-based T_{site} reconstruction for NEEM. (A) Range of T_{site} estimates (shaded region) with mean (dark green line), T_{init} (black line) and OD/YD averages (yellow horizontal lines). A comparison to GCM simulated temperatures is shown in Fig. 1 of the main text. **(B)** Range of A estimates (shaded region) with mean (dark green line), A_{init} (black line) and GCM accumulation (red line). **(C)** Range of δ^{15}N model solutions (shaded region) with mean (dark green line) and δ^{15}N data (black dots).

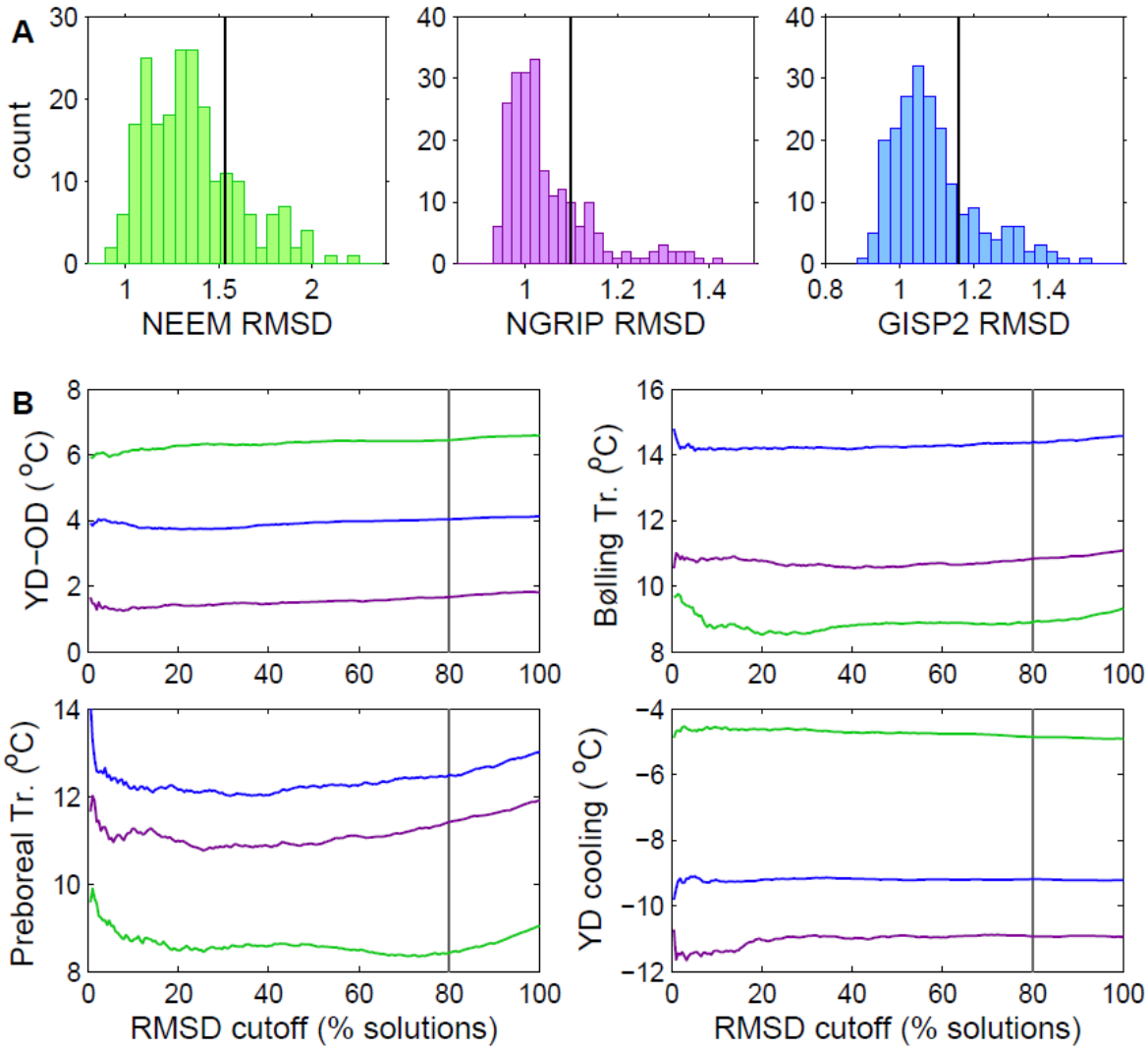

Figure S6: Sensitivity of key results to RMSD cutoff. (A) RMSD distribution of the 216 solutions with cutoff (black vertical line). **(B)** Sensitivity of reconstructed climatic transitions on RMSD cutoff value. We have chosen the RMSD cutoff such that the 20% of the solutions with the poorest fit to the data are rejected (black vertical lines); choosing a different percentage of discarded solutions does not notably change the result in most cases.

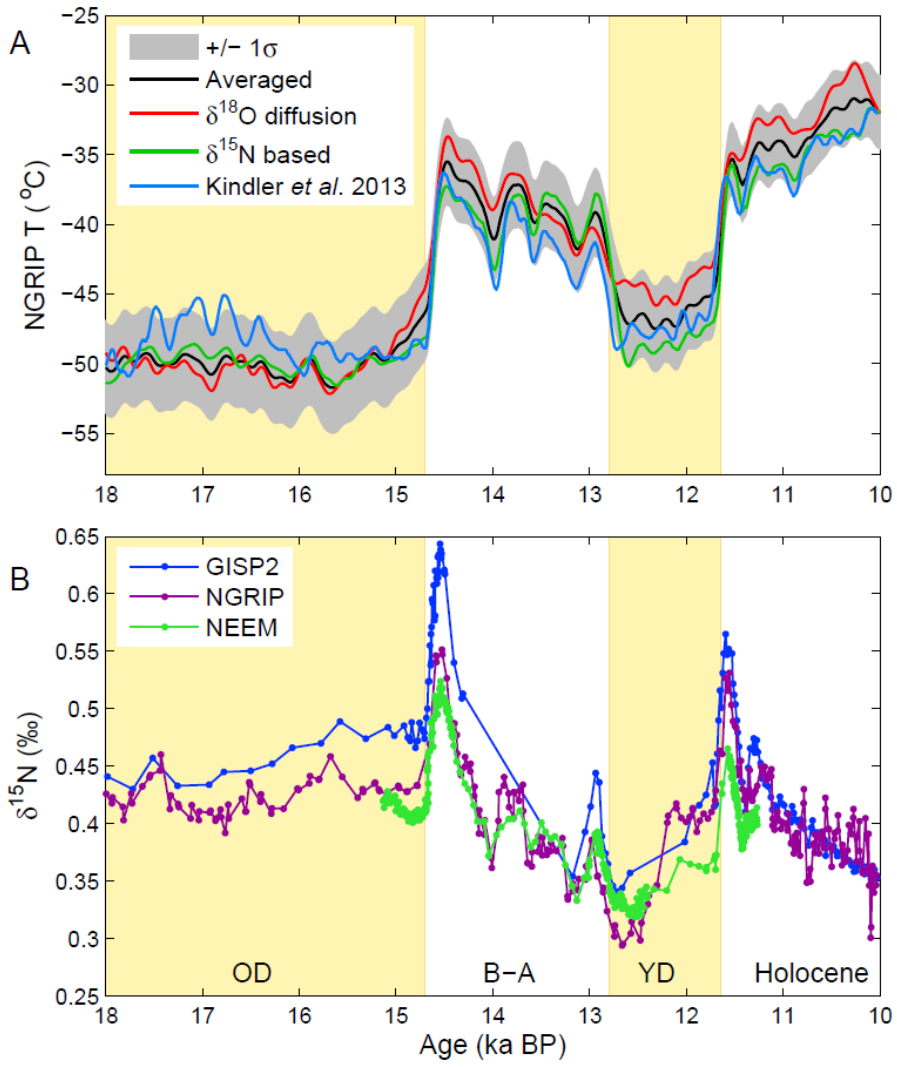

Figure S7: Comparison of NGRIP T_{site} reconstructions. (A) The $\delta^{15}N$ (green) and ^{18}O diffusion-based (red) reconstructions, their average (black) with 1σ uncertainty estimate (shaded) and the reconstruction by Kindler *et al.* (*20*) with 3°C subtracted to match the other reconstructions (blue). The Kindler reconstruction has been converted to the GICC'05 chronology (*58, 62, 102*). **(B)** Raw $\delta^{15}N$ timeseries for the three sites.

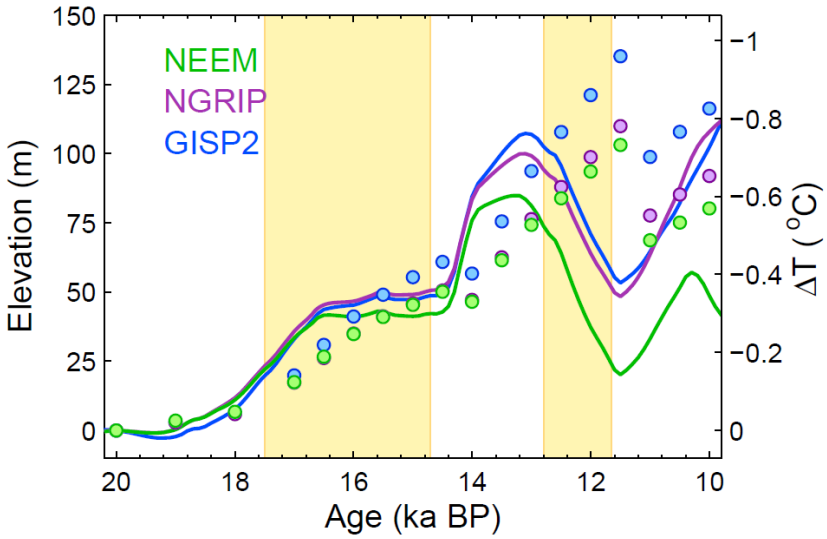

Figure S8: Modeled changes in Greenland ice sheet surface elevation. Surface elevation changes corrected for glacial isostatic adjustment (left axis) and corresponding temperature change (right axis) at GISP2 (blue), NGRIP (purple) and NEEM (green) from the Simpson *et al.*(solid lines) and ICE-5G (round markers) reconstructions (*71, 72*). Changes are relative to 20 ka bp.

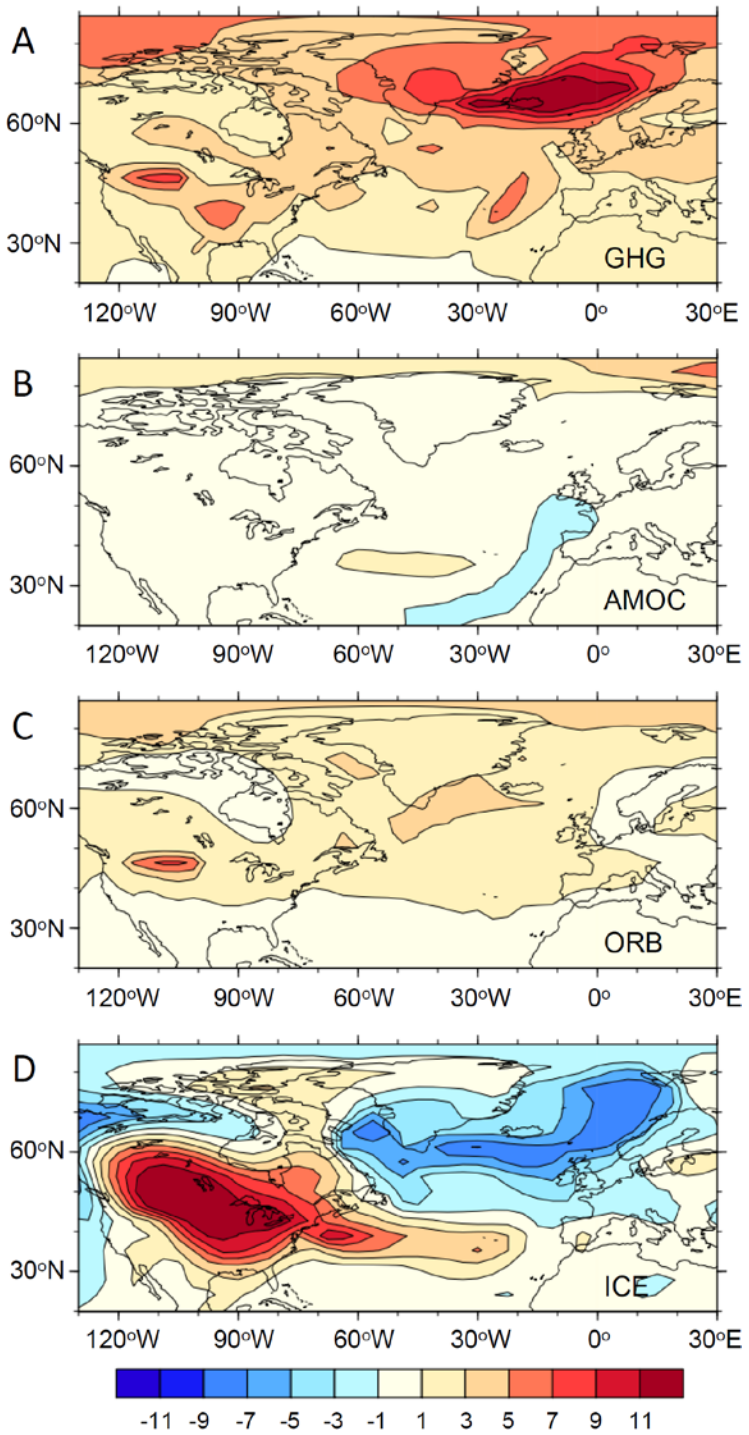

Figure S9: The YD-OD SAT difference using single forcing transient GCM runs. (A) Greenhouse gas forcing only. **(B)** Meltwater fluxes only. **(C)** Orbital (insolation) forcing only. **(D)** Ice sheet orography only.

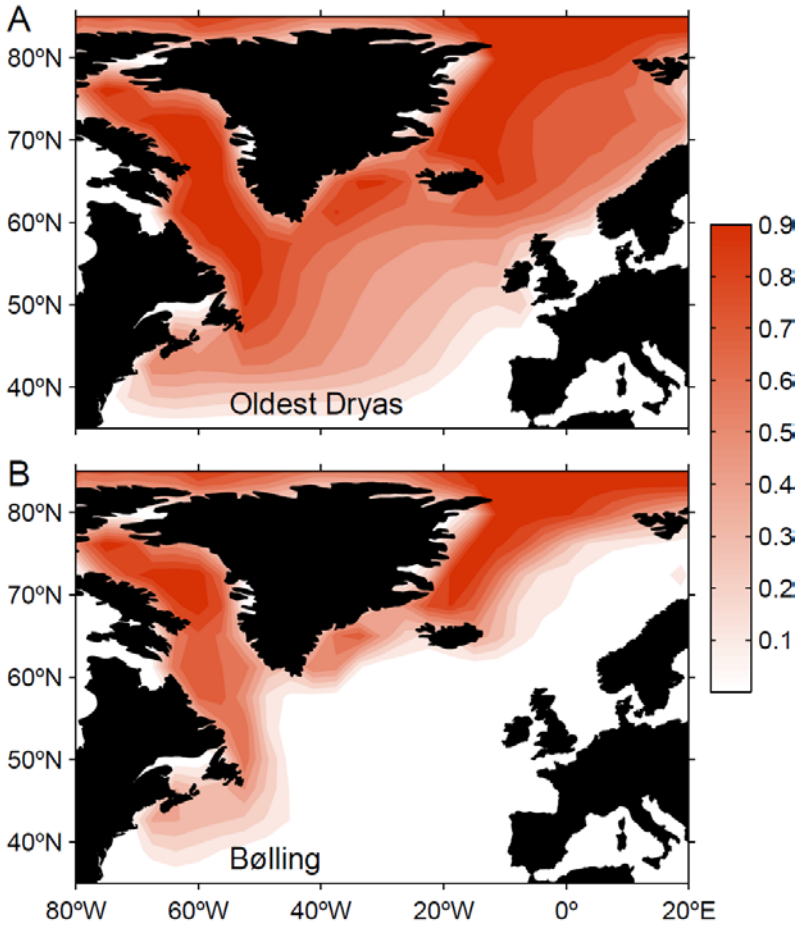

Figure S10: changes in GCM sea ice extent for the Bølling transition. Contour plot of annual mean sea ice fraction. The fraction indicates the area actually covered by sea ice, which is averaged over the year. So an area with 100% sea ice cover for only half of the year, and an area with 50% sea ice cover for an entire year, would both have a mean annual fraction of 0.5. **(A)** prior to the transition (14.9-14.7 ka bp) and **(B)** after the transition (14.4-14.2 ka bp).

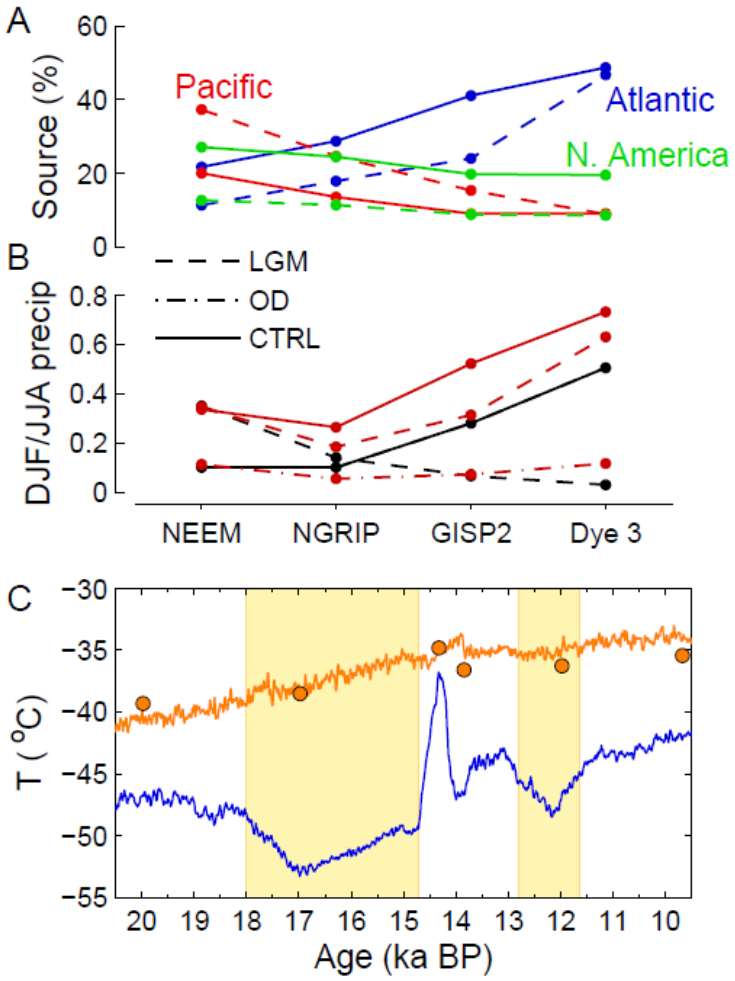

Figure S11: Non-temperature influences on $\delta^{18}O$. (A) Modeled changes in vapor origin between present day (CTRL, solid) and LGM (dashed) using the CCM3 atmospheric GCM (*8*). **(B)** Modeled changes in the ratio of winter (DJF) over summer (JJA) precipitation using the CCM3 GCM (black) from (*8*), and the CCSM3 GCM (red) from (*16*, *17*); indicated periods are present day (CTRL, solid), LGM (dashed) and OD (dot-dashed, CCSM3 only). **(C)** GCM simulated GISP2 temperature (blue), monthly precipitation weighted GISP2 temperature (orange line), and daily precipitation weighted GISP2 temperature (orange dots, with 5°C subtracted).

	YD-OD	Bølling Tr.	YD cooling	Holocene Tr.
T_{site} reconstruction	16.5 to 15.5 vs. 12.5 to 12.0	14.9 to 14.7 vs. 14.55 to 14.35	13.5 to 13.3 vs. 12.5 to 12.3	11.9 to 11.7 vs. 11.2 to 11.0
GCM simulations	16.5 to 15.5 vs. 12.5 to 12.0	14.9 to 14.7 vs. **14.4 to 14.2**	13.5 to 13.3 vs. 12.2 to 12.0	11.9 to 11.7 vs. **11.0 to 10.8**

Table S1: Time intervals used in the evaluations. All values are given in ka bp (with the year 1950 C.E. as zero age); for each transition the mean value over the first interval was subtracted from the mean value over the second interval. Where the intervals used for the T_{site} and GCM evaluation differ, values are marked in **red**.

	YD-OD	Bølling Tr.	YD cooling	Holocene Tr.
δ^{15}N this study	1.7 ± 1.3	10.8 ± 2.0	-10.9 ± 2.0	11.4 ± 3.2
δ^{18}O diffusion	5.9 ± 4.5	11.4 ± 4.7	-5.3 ± 5.0	10.4 ± 4.9
Arithmetic mean	**3.8 ± 2.3**	**11.1 ± 2.6**	**-8.1 ± 2.7**	**10.9 ± 2.9**
Weighted mean	2.0 ± 1.3	10.9 ± 1.8	-10.1 ± 1.9	11.1 ± 2.7
δ^{15}N Kindler	1.5	11.6	-6.2	10.7

Table S2: Comparison of NGRIP temperature reconstructions. All values are given in ^{o}C. Arithmetic and weighted means are given by $\bar{x}_a = \frac{1}{2}(x_1 + x_2)$ and $\bar{x}_w = (\sigma_1^{-2}x_1 + \sigma_2^{-2}x_2)/(\sigma_1^{-2} + \sigma_2^{-2})$, respectively, where x_i give the values obtained by the two individual reconstruction methods, and σ_i give the corresponding uncertainties. Uncertainties in the mean values are calculated using $\bar{\sigma}_a = \frac{1}{2}(\sigma_1^2 + \sigma_2^2)^{\frac{1}{2}}$ and $\bar{\sigma}_w = (\sigma_1^{-2} + \sigma_2^{-2})^{-\frac{1}{2}}$.

	Δage (year)	δ^{15}N (‰)	CZ (m)	$T_{observed}$ (^{o}C)	$T_{reconstr.}$ (^{o}C)	$A_{observed}$ (m a^{-1})	$A_{reconstr.}$ (m a^{-1})
GISP2	190	0.312	5	-31.4	-30.6	0.24	0.23
NGRIP	236	0.310	2	-31.1	-31.9	0.18	0.17
NEEM	188	0.288	4	-28.9	-29.3	0.22	0.21

Table S3: Investigating calibration offsets for the present day.

Additional Author notes: C.B. and V.G. conducted the temperature reconstructions and conceived the study; C.B. drafted the manuscript; J.S., P.K. and M.L. generated and evaluated δ^{15}N data; B.V., V.M.-D. and J.W. generated and evaluated NEEM δ^{18}O data; F.H., A.C., Z.L. and B.O.-B. conceived and performed the GCM simulations; B.L. modeled ice sheet elevation changes; E.B., J.S. and J.W. led the U.S. contribution to the NEEM project; all authors critically reviewed and contributed to the manuscript.

References

34. J. P. Severinghaus, A. Grachev, M. Battle, Thermal fractionation of air in polar firn by seasonal temperature gradients. *Geochem. Geophys. Geosyst.* **2**, art. no. (2001).
35. H. Craig, Y. Horibe, T. Sowers, Gravitational Separation of Gases and Isotopes in Polar Ice Caps. *Science* **242**, 1675 (1988).
36. J. Schwander, in *The Environmental record in glaciers and ice sheets*, H. Oescher, C. C. Langway, Eds. (John Wiley, New York, 1989), pp. 53-67.
37. T. Sowers, M. Bender, D. Raynaud, Y. S. Korotkevich, δ15N of N2 in air trapped in polar ice: A tracer of gas transport in the firn and a possible constraint on ice age-gas age differences. *J. Geophys. Res.* **97**, 15683 (1992).
38. J. P. Severinghaus, T. Sowers, E. J. Brook, R. B. Alley, M. L. Bender, Timing of abrupt climate change at the end of the Younger Dryas interval from thermally fractionated gases in polar ice. *Nature* **391**, 141 (1998).
39. M. C. Leuenberger, C. Lang, J. Schwander, Delta(15)N measurements as a calibration tool for the paleothermometer and gas-ice age differences: A case study for the 8200 BP event on GRIP ice. *J. Geophys. Res.* **104**, 22163 (1999).
40. A. Landais *et al.*, Quantification of rapid temperature change during DO event 12 and phasing with methane inferred from air isotopic measurements. *Earth Planet. Sci. Lett.* **225**, 221 (2004).
41. K. Kawamura *et al.*, Convective mixing of air in firn at four polar sites. *Earth Planet. Sci. Lett.* **244**, 672 (2006).
42. T. Sowers, M. Bender, D. Raynaud, Elemental and isotopic composition of occluded O2 and N2 in polar ice. *J. Geophys. Res.* **94**, 5137 (1989).
43. V. V. Petrenko, J. P. Severinghaus, E. J. Brook, N. Reeh, H. Schaefer, Gas records from the West Greenland ice margin covering the Last Glacial Termination: a horizontal ice core. *Quat. Sci. Rev.* **25**, 865 (2006).
44. T. Kobashi, J. P. Severinghaus, K. Kawamura, Argon and nitrogen isotopes of trapped air in the GISP2 ice core during the Holocene epoch (0-11,500 B.P.): Methodology and implications for gas loss processes. *Geochim. Cosmochim. Acta* **72**, 4675 (2008).
45. J. L. Rosen *et al.*, An ice core record of near-synchronous global climate changes at the Bolling transition. *Nat. Geosci.* **7**, 459 (2014).
46. C. Huber, M. Leuenberger, Measurements of isotope and elemental ratios of air from polar ice with a new on-line extraction method. *Geochem. Geophys. Geosyst.* **5**, 13 (2004).
47. P. M. Grootes, M. Stuiver, J. W. C. White, S. Johnsen, J. Jouzel, Comparison of oxygen isotope records from the GISP2 and GRIP Greenland ice cores. *Nature* **366**, 552 (1993).
48. NGRIP-community-members, High-resolution record of Northern Hemisphere climate extending into the last interglacial period. *Nature* **431**, 147 (2004).
49. NEEM-community-members, Eemian interglacial reconstructed from a Greenland folded ice core. *Nature* **493**, 489 (2013).
50. M. M. Herron, C. C. Langway, Firn densification: An empirical model. *J. Glaciol.* **25**, 373 (1980).
51. J. M. Barnola, P. Pimienta, D. Raynaud, Y. S. Korotkevich, CO2-climate relationship as deduced from the Vostok ice core: a re-examination based on new measurements and on a re-evaluation of the air dating. *Tellus* **43**, 83 (1991).
52. P. Pimienta, P. Duval, Rate controlling processes in the creep of polar glacier ice. *Journal De Physique* **48**, 243 (1987).
53. L. Arnaud, J. M. Barnola, P. Duval, in *Physics of Ice Core Records*, T. Hondoh, Ed. (2000), pp. 285-305.
54. J. Schwander *et al.*, Age scale of the air in the summit ice: Implication for glacial-interglacial temperature change. *J. Geophys. Res.* **102**, 19483 (1997).
55. P. Martinerie *et al.*, Air content paleo record in the Vostok ice core (Antarctica): A mixed record of climatic and glaciological parameters. *J. Geophys. Res.* **99**, 10565 (1994).

56. C. Buizert, T. Sowers, T. Blunier, Assessment of diffusive isotopic fractionation in polar firn, and application to ice core trace gas records. *Earth Planet. Sci. Lett.* **361**, 110 (2013).
57. M. W. Hörhold *et al.*, On the impact of impurities on the densification of polar firn. *Earth Planet. Sci. Lett.* **325–326**, 93 (2012).
58. S. O. Rasmussen *et al.*, A new Greenland ice core chronology for the last glacial termination. *J. Geophys. Res.* **111**, D06102 (2006).
59. S. O. Rasmussen *et al.*, A first chronology for the North Greenland Eemian Ice Drilling (NEEM) ice core. *Clim. Past* **9**, 2713 (2013).
60. K. M. Cuffey, W. S. B. Paterson, *The physics of glaciers, 4th edition*. (Butterworth-Heinemann, Oxford, UK, 2010), pp. 693.
61. K. M. Cuffey, R. B. Alley, P. M. Grootes, J. M. Bolzan, S. Anandakrishnan, Calibration of the δ18O isotopic paleothermometer for central Greenland, using borehole temperatures. *J. Glaciol.* **40**, 341 (1994).
62. K. K. Andersen *et al.*, The Greenland Ice Core Chronology 2005, 15-42 ka. Part 1: constructing the time scale. *Quat. Sci. Rev.* **25**, 3246 (2006).
63. N. S. Gundestrup, D. Dahl-Jensen, B. L. Hansen, J. Kelty, Bore-hole survey at Camp Century, 1989. *Cold Regions Sci. Technol.* **21**, 187 (1993).
64. C. Buizert *et al.*, Gas transport in firn: multiple-tracer characterisation and model intercomparison for NEEM, Northern Greenland. *Atmos. Chem. Phys.* **12**, 4259 (2012).
65. G. B. Dreyfus *et al.*, Firn processes and [delta]15N: potential for a gas-phase climate proxy. *Quat. Sci. Rev.* **29**, 28 (2010).
66. K. Fuhrer, A. Neftel, M. Anklin, V. Maggi, Continuous measurements of hydrogen peroxide, formaldehyde, calcium and ammonium concentrations along the new GRIP ice core from Summit, Central Greenland. *Atmos. Environ.* **27**, 1873 (1993).
67. K. A. Kaspers *et al.*, Model calculations of the age of firn air across the Antarctic continent. *Atmos. Chem. Phys.* **4**, 1365 (2004).
68. D. Dahl-Jensen *et al.*, Past Temperatures Directly from the Greenland Ice Sheet. *Science* **282**, 268 (1998).
69. K. M. Cuffey *et al.*, Large Arctic Temperature Change at the Wisconsin-Holocene Glacial Transition. *Science* **270**, 455 (1995).
70. E. Witrant *et al.*, A new multi-gas constrained model of trace gas non-homogeneous transport in firn: evaluation and behaviour at eleven polar sites. *Atmos. Chem. Phys.* **12**, 11465 (2012).
71. M. J. R. Simpson, G. A. Milne, P. Huybrechts, A. J. Long, Calibrating a glaciological model of the Greenland ice sheet from the Last Glacial Maximum to present-day using field observations of relative sea level and ice extent. *Quat. Sci. Rev.* **28**, 1631 (2009).
72. W. Peltier, Global glacial isostasy and the surface of the ice-age Earth: the ICE-5G (VM2) model and GRACE. *Annu. Rev. Earth Planet. Sci.* **32**, 111 (2004).
73. L. Tarasov, W. Richard Peltier, Greenland glacial history and local geodynamic consequences. *Geophys. J. Int.* **150**, 198 (2002).
74. B. S. Lecavalier *et al.*, Revised estimates of Greenland ice sheet thinning histories based on ice-core records. *Quat. Sci. Rev.* **63**, 73 (2013).
75. K. Steffen, J. Box, Surface climatology of the Greenland Ice Sheet: Greenland Climate Network 1995–1999. *J. Geophys. Res.* **106**, 33951 (2001).
76. C. Li, D. S. Battisti, C. M. Bitz, Can North Atlantic Sea Ice Anomalies Account for Dansgaard–Oeschger Climate Signals?*. *J. Clim.* **23**, 5457 (2010).
77. S. V. Petersen, D. P. Schrag, P. U. Clark, A new mechanism for Dansgaard-Oeschger cycles. *Paleoceanography*, n/a (2013).
78. A. C. Clement, L. C. Peterson, Mechanisms of abrupt climate change of the last glacial period. *Rev. Geophys.* **46**, (2008).
79. H. Gildor, E. Tziperman, Sea ice as the glacial cycles' climate switch: Role of seasonal and orbital forcing. *Paleoceanography* **15**, 605 (2000).

80. Y. Kaspi, R. Sayag, E. Tziperman, A "triple sea-ice state" mechanism for the abrupt warming and synchronous ice sheet collapses during Heinrich events. *Paleoceanography* **19**, PA3004 (2004).
81. T. M. Dokken, K. H. Nisancioglu, C. Li, D. S. Battisti, C. Kissel, Dansgaard-Oeschger cycles: Interactions between ocean and sea ice intrinsic to the Nordic seas. *Paleoceanography* **28**, 491 (2013).
82. D. J. R. Thornalley, S. Barker, W. S. Broecker, H. Elderfield, I. N. McCave, The Deglacial Evolution of North Atlantic Deep Convection. *Science* **331**, 202 (2011).
83. P. U. Clark, N. G. Pisias, T. F. Stocker, A. J. Weaver, The role of the thermohaline circulation in abrupt climate change. *Nature* **415**, 863 (Feb, 2002).
84. S. Barker *et al.*, Interhemispheric Atlantic seesaw response during the last deglaciation. *Nature* **457**, 1097 (Feb, 2009).
85. N. L. Roberts, A. M. Piotrowski, J. F. McManus, L. D. Keigwin, Synchronous Deglacial Overturning and Water Mass Source Changes. *Science* **327**, 75 (2010).
86. T. M. Dokken, E. Jansen, Rapid changes in the mechanism of ocean convection during the last glacial period. *Nature* **401**, 458 (1999).
87. C. Wunsch, Abrupt climate change: An alternative view. *Quat. Res.* **65**, 191 (2006).
88. G. Knorr, G. Lohmann, Southern Ocean origin for the resumption of Atlantic thermohaline circulation during deglaciation. *Nature* **424**, 532 (2003).
89. J. Jouzel *et al.*, Validity of the temperature reconstruction from water isotopes in ice cores. *J. Geophys. Res.* **102**, 26471 (1997).
90. V. Masson-Delmotte *et al.*, Abrupt change of Antarctic moisture origin at the end of Termination II. *Proc. Natl. Acad. Sci. U. S. A.* **107**, 12091 (2010).
91. J. P. Steffensen *et al.*, High-resolution Greenland Ice Core data show abrupt climate change happens in few years. *Science* **321**, 680 (2008).
92. L. C. Sime *et al.*, Warm climate isotopic simulations: what do we learn about interglacial signals in Greenland ice cores? *Quat. Sci. Rev.* **67**, 59 (2013).
93. C. D. Charles, D. Rind, J. Jouzel, R. D. Koster, R. G. Fairbanks, Seasonal Precipitation Timing and Ice Core Records. *Science* **269**, 247 (1995).
94. G. Krinner, M. Werner, Impact of precipitation seasonality changes on isotopic signals in polar ice cores: a multi-model analysis. *Earth Planet. Sci. Lett.* **216**, 525 (2003).
95. G. Krinner, C. Genthon, J. Jouzel, GCM analysis of local influences on ice core δ signals. *Geophys. Res. Lett.* **24**, 2825 (1997).
96. L. C. Sime, J. C. Tindall, E. W. Wolff, W. M. Connolley, P. J. Valdes, Antarctic isotopic thermometer during a CO2 forced warming event. *J. Geophys. Res.* **113**, D24119 (2008).
97. CLIMAP-project-members, The surface of the ice-age Earth. *Science* **191**, 1131 (1976).
98. M. Werner, M. Heimann, G. Hoffmann, Isotopic composition and origin of polar precipitation in present and glacial climate simulations. *Tellus* **53**, 53 (2001).
99. H. C. Steen-Larsen *et al.*, Understanding the climatic signal in the water stable isotope records from the NEEM shallow firn/ice cores in northwest Greenland. *J. Geophys. Res.* **116**, D06108 (2011).
100. A. Persson, P. L. Langen, P. Ditlevsen, B. M. Vinther, The influence of precipitation weighting on interannual variability of stable water isotopes in Greenland. *J. Geophys. Res.* **116**, D20120 (2011).
101. H. C. Steen-Larsen *et al.*, What controls the isotopic composition of Greenland surface snow? *Clim. Past* **10**, 377 (2014).
102. A. Svensson *et al.*, The Greenland Ice Core Chronology 2005, 15-42 ka. Part 2: comparison to other records. *Quat. Sci. Rev.* **25**, 3258 (Dec, 2006).